

Chapter 7

Mesoscopic pn Junction - Coulomb Blockade, Squeezing and Single Photon Generation -

In the previous chapter, we have presented the detailed theory on a pn junction driven by a constant voltage source, while only a phenomenological argument was given for the constant current operation of a pn junction. A noise equivalent circuit allows us to calculate the junction current and junction voltage noise spectra. Under constant current operation ($R_s \gg R_d$), the junction current noise features a sub-shot noise spectrum $S_{i_n}(\omega) = \frac{4k_B\theta}{R_s} < 2qI$ but the junction voltage noise has a full shot noise $S_{v_n}(\omega) = 2qIR_d^2$. The opposite is true for constant voltage operation.

In this chapter we will develop a microscopic theory for the constant current operation of a pn junction, which takes into account the Coulomb blockade effect for a discrete thermionic emission process[1]. We will show the experimental evidence for the sub-shot noise (squeezing) behaviour of emitted photons from such a pn junction as a proof of the theory[2]. When a pn junction size decreases, a single electron charging energy $q^2/2C$ eventually exceeds thermal energy $k_B\theta$, and we expect a single electron is thermionically emitted one by one with a regulated time interval $\tau = q/I$. This should result in generation of regulated single photons with the same interval. This single electron thermionic emission (or tunneling) oscillation has not been observed experimentally yet due to the difficulty of biasing such a small junction by a high-impedance constant current source[3].

However, single photon turnstile device based on periodically modulated constant voltage source has been proposed[4] and demonstrated[5] as an alternative means to generate regulated electron-hole pair injection and single photon emission.

7.1 Coulomb Blockade Effect in a pn Junction

Consider a P - p^+ - I - N double-heterojunction diode, as shown in Fig. 7.1. An undoped I -layer has a thickness of x_u and the depletion layer of an N -layer has a varying thickness $x_n(t)$. The forward thermionic emission of an electron from the N -layer across the

depletion layer has an average rate of[6]

$$\kappa(t) = \frac{A\theta^2 A^*}{q} \exp \left[-\frac{V_d - V(t)}{V_T} \right] \quad , \quad (7.1)$$

where A is an effective cross-section of a junction, A^* is the Richardson constant, $V(t)$ is the junction voltage, and V_d is an “effective” built-in potential given by[1]

$$V_d = V_D + \frac{q}{2C_{\text{dep}}} \quad . \quad (7.2)$$

where V_D is the standard built-in potential. The second term on the right-hand-side of Eq. (7.2) represents a single-electron charging energy, which is neglected in the previous chapter because a macroscopic pn junction has a large junction capacitance C_{dep} and satisfies $q^2/2C_{\text{dep}} \ll k_B\theta$. This term simply offsets an effective junction voltage by a small amount ($q/2C_{\text{dep}}$) in the constant-voltage bias case, but plays a crucial role in the constant-current bias case. Here, one assumes that the forward bias voltage is very small and that the backward thermionic emission of an electron from the p^+ -layer to the N -layer is negligible due to a high potential barrier and a low electron density in the p^+ -layer. This assumption is valid unless a very strong forward bias is applied to the junction. The effective potential barrier from the N -layer to the p^+ -layer, $V_d - V(t)$, is a function of the charge in the depletion layer:

$$V_d - V(t) = \underbrace{\frac{qN_D}{\varepsilon_2} x_u x_n(t)}_{\substack{\uparrow \\ \text{potential barrier} \\ \text{in the } I \text{ layer}}} + \underbrace{\frac{qN_D}{2\varepsilon_2} x_n^2(t)}_{\substack{\uparrow \\ \text{potential barrier} \\ \text{in the depleted } N \text{ layer}}} \quad . \quad (7.3)$$

Here, N_D is the ionized donor concentration in the N -layer.

There are two competing processes which change $x_n(t)$ and $V(t)$: “discrete” thermionic emission of an electron across the depletion layer from the N -layer to the p^+ -layer and “continuous” charging via a constant external circuit current I . The former decreases $V(t)$ abruptly and the latter increases $V(t)$ continuously.

When a single electron is emitted from the N -layer to the p^+ -layer, both electron gas in the N -layer and hole gas in the p^+ -layer must take back from the junction in order to satisfy the charge neutrality condition in the bulk N - and p^+ -layers. This results in an increase in the surface charge in the depletion layer by $+q$ in the N -side and $-q$ in the p^+ -side. The shift of the electron gas edge by such a single-electron thermionic emission event is

$$\Delta x_n = \frac{1}{N_D A} \quad . \quad (7.4)$$

The corresponding decrease in the junction voltage is

$$\Delta V = -\frac{qN_D}{\varepsilon_2} x_u \Delta x_n = -\frac{q}{C_{\text{dep}}} \quad , \quad (7.5)$$

where the depletion layer capacitance is approximated by

$$C_{\text{dep}} \simeq \frac{\varepsilon_2 A}{x_u} \quad . \quad (7.6)$$

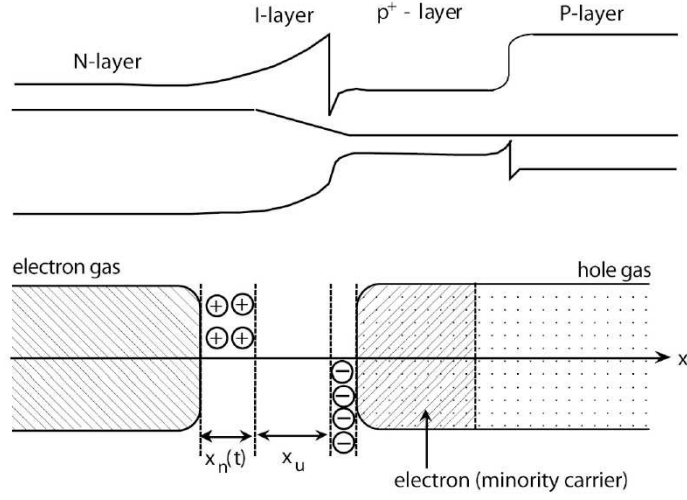


Figure 7.1: A $P-p^+-I-N$ double-heterostructure diode.

In order for an electron to be thermionically emitted across the depletion layer, the electron must have an excess energy $q^2/2C_{\text{dep}}$ above the effective potential barrier because of the increase in depletion layer width. The depletion layer width and the potential barrier increase during an electron's transit across it. This is the physical meaning of the second term of the right-hand-side of Eq. (7.2). The thermionic emission rate $\kappa(t)$ is abruptly decreased by a single-electron thermionic emission event:

$$\begin{aligned}\kappa(t_+) &= \kappa(t_-) \exp\left(-\frac{q}{C_{\text{dep}}V_T}\right) \\ &= \kappa(t_-) \exp(-r) \quad ,\end{aligned}\tag{7.7}$$

where

$$r = \frac{(q^2/C_{\text{dep}})}{k_B\theta} \quad .\tag{7.8}$$

The parameter r is the ratio of the single-electron charging energy and the characteristic energy of thermal fluctuation.

An external circuit current I pushes the electron and hole gases toward the junction continuously:

$$\frac{d}{dt}x_n(t) = -\frac{I}{qN_D A} \quad .\tag{7.9}$$

The decrease in the depletion layer width $x_n(t)$ is therefore a linear function of t , and thus the decrease in the effective potential barrier is also a linear function of time:

$$\begin{aligned}\frac{d}{dt}[V_d - V(t)] &= -\frac{qN_D}{\epsilon_2}x_u\Delta x_n(t) \\ &= -\frac{I}{C_{\text{dep}}}t \quad ,\end{aligned}\tag{7.10}$$

which results in the exponential increase of the thermionic emission rate

$$\begin{aligned}\kappa(t) &= \kappa(0) \exp \left[\frac{I}{C_{\text{dep}} V_T} t \right] \\ &= \kappa(0) \exp \left(\frac{r}{\tau} t \right) \quad ,\end{aligned}\tag{7.11}$$

where the parameter r is defined by Eq. (7.8) and τ is the single-electron charging time by the circuit current:

$$\tau = \frac{q}{I} \quad .\tag{7.12}$$

The time constant τ/r determines how quickly the thermionic emission rate increases and is termed a ‘‘thermionic emission time τ_{te} .’’ When $\kappa(t)$ reaches $1/\tau_{te}$ at $t = 0$ by continuous charging, the thermionic emission event is likely to occur by this time because the probability for a single electron to be emitted is

$$P = \int_{-\infty}^0 \kappa(t') dt' = \int_{-\infty}^0 \frac{1}{\tau_{te}} e^{t'/\tau_{te}} dt' = 1 \quad .\tag{7.13}$$

Since $\kappa(0)\tau_{te} = 1$, this thermionic emission should occur in a short time interval τ_{te} centered at $t = 0$, as shown in Fig. 7.2. The thermionic emission time τ_{te} is represented in terms of the differential resistance $R_d = \frac{V_T}{I}$ and the depletion-layer capacitance C_{dep} :

$$\tau_{te} = \frac{\tau}{r} = C_{\text{dep}} R_d \quad .\tag{7.14}$$

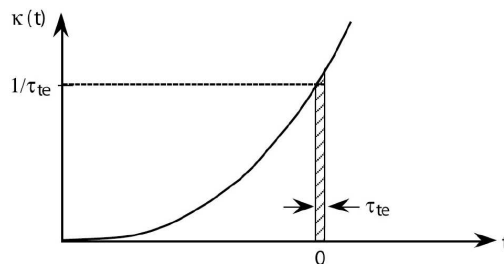


Figure 7.2: A thermionic emission rate $\kappa(t)$ vs. time.

The over-all thermionic emission rate, including the above two competing processes, is given by

$$\kappa(t) = \kappa(0) \exp \left[\frac{t}{\tau_{te}} - r n_e(t) \right] \quad ,\tag{7.15}$$

where $n_e(t)$ is the number of electrons emitted from the N -layer into the p^+ -layer in a time interval $(0, t)$.

There are four distinct regimes of operation for a constant-current-driven pn junction.

(1) Coulomb Blockade Regime or Mesoscopic Regime ($r > 1$)

When the single-electron charging energy q^2/C_{dep} is larger than the thermal energy $k_B\theta$ and the source resistance R_S is larger than q/IC_{dep} , the three relevant time constants, which determine the junction dynamics, satisfy the following relations:

$$\begin{array}{ccccc}
 C_{\text{dep}}R_S & > & \frac{q}{I} & > & C_{\text{dep}}R_d \\
 \nearrow & & \uparrow & & \nwarrow \\
 \text{Circuit Relaxation} & & \text{Single Electron} & & \text{Thermionic Emission} \\
 \text{Time} & & \text{Charging Time } \tau & & \text{Time } \tau_{te} = \frac{\tau}{r} = \frac{k_B\theta C_{\text{dep}}}{qI}
 \end{array} \quad (7.16)$$

In such a case, the junction voltage $V(t)$ and the thermionic emission rate $\kappa(t)$ oscillate with a fixed time interval equal to the single-electron charging time $\tau = q/I$, as shown in Fig. 7.3.

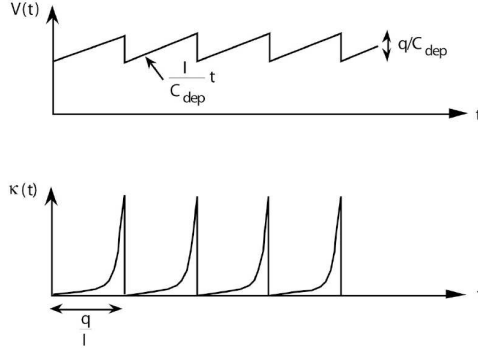


Figure 7.3: A single electron thermionic emission oscillation for $r > 1$.

In a time interval $(0, \tau)$, the junction voltage $V(t)$ increases linearly according to $\frac{I}{C_{\text{dep}}}t$ due to the constant current I , because the circuit relaxation time $C_{\text{dep}}R_S$ is longer than the single-electron charging time τ . Such a linear increase in the junction voltage results in an exponential increase in the thermionic emission rate $\kappa(t) \propto \exp(t/\tau_{te})$. A single-electron thermionic emission event occurs (on average) when $\kappa(t)$ becomes equal to $1/\tau_{te}$ because

$$\int_0^\tau \frac{1}{\tau_{te}} \exp\left(\frac{t' - \tau}{\tau_{te}}\right) dt' \simeq 1 \quad (\tau \gg \tau_{te}) \quad (7.17)$$

The probability for thermionic emission at $t = 0$ is negligibly small, $\kappa(0)\tau = \frac{\tau}{\tau_{te}} e^{-\frac{\tau}{\tau_{te}}} \ll 1$. On the other hand, the probability for thermionic emission between $t = \tau - \frac{\tau_{te}}{2}$ and $t = \tau + \frac{\tau_{te}}{2}$ is close to one, $\kappa(\tau)\tau_{te} = 1$. Therefore, a single-electron thermionic emission event is well regulated at a fixed time $t = \tau, 2\tau, 3\tau, \dots$ within a small jitter of τ_{te} , as shown in Fig. 7.3.

The junction voltage oscillates at a frequency $f = I/q$ and each electron is thermionically emitted with a regulated time interval $\tau = q/I$. This oscillatory behavior is termed a “single-electron thermionic emission (SETE) oscillation.” When $r > 1$ is satisfied, $\tau_{te} < \tau$ is always satisfied, irrespective of the current I , which is a unique feature of SETE oscillation in a pn junction. This is not the case for the single electron tunneling (SET) oscillation in a mesoscopic tunnel junction. In SETE oscillation, the upper and lower bounds on the current are imposed by

$$I > \frac{q}{C_{\text{dep}}R_S} \quad (\text{Constant Current Operation Condition}) \quad , \quad (7.18)$$

$$I < \frac{q}{r\bar{\tau}_f} \quad (\text{Quasi - Equilibrium Distribution Condition}) \quad . \quad (7.19)$$

This last condition is required because the charge distributions in both sides of the depletion layer must reach the steady-state condition by collision with the lattice. This carrier relaxation time must be much faster than the thermionic emission time τ_{te} .

(2) Sub-Poisson Regime ($r < 1, T_{meas} > \tau_{te}$)

When $\frac{q^2}{C_{\text{dep}}}$ is smaller than $k_B\theta$, the Coulomb blockade effect by a single electron is negligibly small. However, if $R_s > R_d$ is satisfied, the pn junction is still driven by a high-impedance constant-current source. The three time constants satisfy the following inequalities:

$$C_{\text{dep}}R_S > C_{\text{dep}}R_d > \frac{q}{I} \quad . \quad (7.20)$$

In such a case, continuous charging of $n_e (= \frac{1}{r} > 1)$ electrons must be completed by the current I or n_e electrons must be thermionically emitted in order for the thermionic emission rate $\kappa(t)$ to be appreciably modulated, as shown in Fig. 7.4.

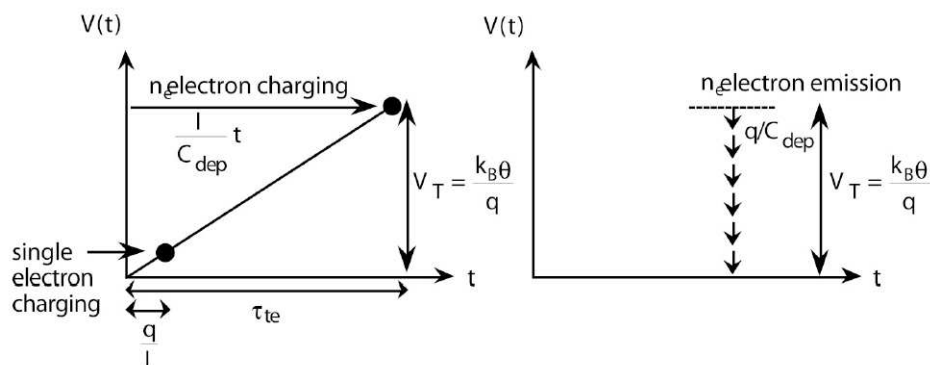


Figure 7.4: A collective Coulomb blockade effect due to continuous charging or sequential thermionic emission of n_e electrons.

In a real situation, the continuous charging and discrete emission of an electron occurs randomly in a microscopic time scale. However, the collective effect of many electrons tend to regulate the thermionic emission events in a macroscopic time scale; that is, more-than-average thermionic emission events are followed by less-than-average thermionic emission events, and *vice versa*. Such a self-feedback mechanism is referred to as a “collective Coulomb blockade effect”. A well-known example of such a collective Coulomb blockade is the sub-shot-noise behavior of a space-charge-limited vacuum tube[7].

The probability of n_e electrons emitted during a time interval T is given by[1]

$$p(n_e, T) = \frac{1}{N} \frac{\bar{n}_e^{n_e} e^{-\bar{n}_e}}{n_e!} \exp \left[-\frac{r}{2} (n_e - \bar{n}_e)^2 \right] , \quad (7.21)$$

where N is the normalization constant and $\bar{n}_e = T/\tau$ is the average number of emitted electrons. The probability Eq. (7.21) is the product of the Poisson distribution with a variance

$$\sigma_{n_e}^2 = \bar{n}_e , \quad (7.22)$$

and the Gaussian distribution with a variance

$$\sigma_{n_e}^2 = \frac{1}{r} = \frac{k_B \theta q^2}{C_{\text{dep}}} . \quad (7.23)$$

Therefore, if T is longer than τ_{te} , then $\bar{n}_e = \frac{T}{\tau}$ becomes larger than $\frac{1}{r} = \frac{\tau_{te}}{\tau}$, and the probability Eq. (7.21) features a sub-Poisson distribution. The average electron number \bar{n}_e is proportional to T , while the variance $\sigma_{n_e}^2$, given by Eq. (7.23), remains constant. Therefore, the noise suppression from the Poisson limit is improved with increasing T .

(3) Poisson Regime ($r < 1, T < \tau_{te}$)

On the other hand, if T is shorter than τ_{te} , the probability Eq. (7.21) approaches a Poisson distribution because the Gaussian distribution becomes broader than the Poisson distribution. Even though a junction is driven by a constant current source, the electron emission obeys a random Poisson-point-process for such a short time interval.

When $1/r > \bar{n}_e$, the variance approaches \bar{n}_e (Poisson limit). On the other hand, when $1/r < \bar{n}_e$, the variance decreases linearly with $1/r$. This is a collective Coulomb blockade regime. Finally, when $1/r < 1$, the variance is suppressed to below a single electron. This is a single-electron Coulomb blockade regime. The power spectral density $S_{n_e}(\omega)$ corresponding to the two regimes of collective Coulomb blockade and single-electron Coulomb blockade are shown in Fig. 7.5. The power spectral density is reduced to below the full-shot noise level at a frequency region below $f = 1/2\pi\tau_{te}$. In the case of $r > 1$, a coherent oscillation peak is observed at $f = \frac{1}{\tau}$ due to single electron thermionic emission oscillation, while, in the case of $r < 1$, a coherent oscillation peak is absent because each individual electron event is not regulated.

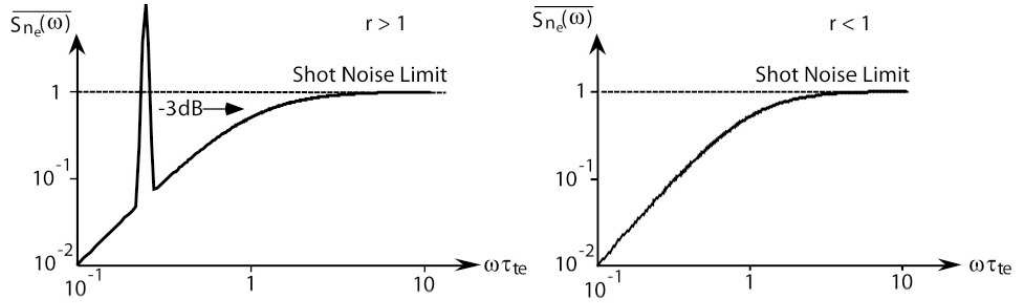


Figure 7.5: The power spectra $S_{n_e}(\omega)$ of thermionically emitted electrons for the two regimes: single electron Coulomb blockade regime ($r > 1$) and collective Coulomb blockade regime ($r < 1$).

(4) Macroscopic Regime ($r \ll 1, \tau_n \gg \tau$)

Thus far the backward emission of electrons from the p^+ -layer to the N -layer has been neglected. This approximation is valid when $\Delta E_c \gg q\phi_n + k_B\theta$, where ϕ_n is a quasi-Fermi level for electrons, measured from the bottom of the conduction band, in the p^+ -layer (Fig. 7.1). However, if the average electron density $n_p = \frac{\tau_n}{\tau AL}$ becomes large enough and the temperature is high enough, the above condition is no longer satisfied. Here, τ_n is the electron lifetime in the p^+ -layer. In such a case, the net thermionic emission rate (forward emission rate – backward emission rate) is not only dependent on the junction voltage $V(t)$, but is also dependent on the electron density n_p .

For instance, one can think of the following two relaxation processes. Suppose that more-than-average recombination (photon emission) events occur in the p -layer at a certain time, resulting in the decrease in n_p , which increases the net thermionic emission rate and decreases the junction voltage V . This drop in V remains for a time interval $\tau_{te} = \frac{\tau}{r}$. Before the steady-state junction voltage \bar{V} and the steady state electron density \bar{n}_p are recovered, the recombination (photon emission) events are less than average. One deterministic process (charging by a constant current) and two stochastic processes (thermionic emission and recombination of electrons) are involved in this relaxation mechanism, which leads to the self-feedback stabilization for recombination and photon emission events.

On the other hand, if recombination events become less than average at a certain time, this results in an increase in n_p , which decreases the net thermionic emission rate and increases V . The increase in V remains for a relatively long time. During this time period, recombination events are more than average. In both cases, the light intensity (proportional to the recombination rate) and the junction voltage (inversely proportional to the net thermionic emission rate) are negatively correlated. Such negative correlation is indeed observed in a sub-Poissonian light emitting pn junction[8].

7.2 Langevin Theory of pn Junction Diodes

The noise associated with injection of carriers into the active region of a light-emitting pn junction determines the intensity noise properties of the light output from these devices. Generation of intensity-squeezed light from a semiconductor laser[9] and sub-Poissonian light from a light-emitting diode (LED)[10] under constant-current driving conditions implies that the carrier injection into the active region can be regulated to well below the Poissonian limit.

We have demonstrated in chapter 5 that an electron flow in the presence of elastic scatterings features reduced shot noise, but still much larger than thermal noise. Suppression of current shot noise (generation of “quiet electron flow”) in a macroscopic resistor has been attributed to inelastic electron scatterings. Although the noise generated in the external resistor is far below the shot-noise level, this does not mean that the carrier injection into the active region of a pn junction is regulated. In fact, it has been found in the previous section using a microscopic thermionic emission model that the carriers are injected stochastically across the depletion layer. The charging energy at the junction, however, plays a key role in establishing the correlation between successive carrier-injection events, thereby regulating this stochasticity.

In this section, a rather general Langevin theory of pn junction light-emitting diodes in the macroscopic regime is presented. The charging energy of carriers across the depletion layer is taken into account through the Poisson equation at the junction. The resulting carrier dynamics is analyzed by a set of Langevin equations. The noise spectra and correlation spectra of the generated photon field, external circuit current, junction voltage and carrier number in the active region can be calculated using this formalism. This model provides a complete understanding of the noise properties of pn junction light-emitting devices in the macroscopic limit, including the sub-Poissonian light generated by a semiconductor LED.

7.2.1 Junction Voltage Dynamics: the Poisson Equation

Here, it is assumed that the junction current is mainly carried by the injection of electrons into the p-type layer and subsequent radiative recombination, so that the optically active region is formed in the p-type layer. Under this assumption, it is natural to define the active medium to be the region in the p-type layer where injected electrons recombine with holes. It is further assumed that there is no carrier recombination within the depletion layer. The situation is illustrated in Fig. 7.6, where the two cases of a homojunction and a heterojunction are shown. Throughout the analysis, it is assumed that (a) the carrier thermalization rate by phonon scattering is larger than any other rate, so that the electrons are always in quasi-equilibrium (b) the recombination lifetime (τ_{sp}) is short, so that the major current-flow mechanism is the radiative recombination of minority carriers.

The Poisson equation is given by

$$\nabla^2 V = -\rho / \epsilon \quad , \quad (7.24)$$

where ρ is the space charge density and ϵ is the dielectric constant of the material. Integration of this equation gives

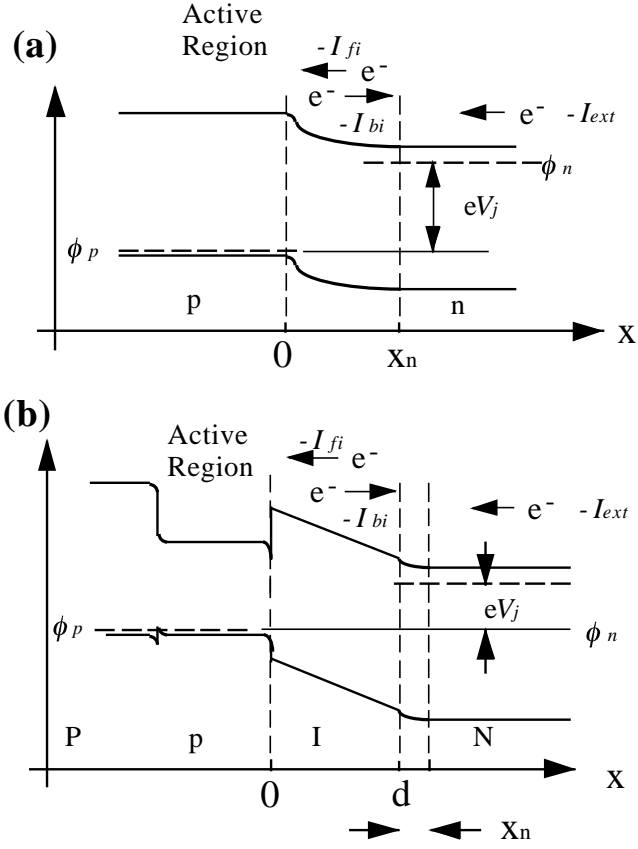


Figure 7.6: Schematic of the junction and the parameters considered. Arrows indicate the direction of electron flow. (a) pn homojunction; (b) p-i-n heterojunction

$$\frac{dV_j}{dt} = \frac{1}{C_{dep}} I_{ext}(t) \quad , \quad (7.25)$$

which describes the dynamics of the junction voltage $V_j(t)$, which is defined by the difference between the quasi-Fermi levels of the n-type layer (ϕ_n) and the p-type layer (ϕ_p) at the junction.

First, consider an abrupt pn homojunction (Fig. 7.6(a)) where the depletion layer is formed within the uniformly doped layer. If V_1 is the junction potential supported by the n-type layer and V_2 is that supported by the p-type layer, the total potential V_{tot} supported by the junction is given by $V_{tot} = V_1 + V_2$. In the limit of an one-sided junction where the doping level of the p-type layer is much higher than that of the n-type layer, $V_2 \ll V_1$. Integrating Eq. (7.24) gives the junction voltage V_j as

$$V_j = V_{bi} - V_{tot} = \frac{qN_D}{2\epsilon} (x_{n0}^2 - x_n^2) \quad . \quad (7.26)$$

Here, the space charge density ρ is given by the doping density eN_D . V_{bi} is the built-in potential, x_{n0} and x_n are the width of the depletion layer at zero bias and at finite bias V_j , respectively.

The space charge separated by the junction, Q , can be defined in terms of the width of the depletion layer and is given by $Q \equiv eN_D A_0 x_n$, where A_0 is the cross-sectional area of the junction. The depletion layer capacitance is defined by

$$C_{dep} \equiv \left| \frac{dQ}{dV_j} \right| = \frac{\epsilon A_0}{x_n} \quad . \quad (7.27)$$

The rate of change of Q is equal to the circuit current $I_{ext}(t)$,

$$I_{ext}(t) \equiv -\frac{dQ}{dt} = -qN_D A_0 \frac{dx_n}{dt} \quad . \quad (7.28)$$

The case of a p-I-N heterojunction (Fig. 7.6(b)) is described in a similar way:

$$V_j = \frac{qN_D}{2\epsilon} [x_{n0}^2 - x_n^2 + 2d(x_{n0} - x_n)] \quad , \quad (7.29)$$

where d is the intrinsic layer width and x_n is the depletion layer width in the n-type layer. Equation (7.25) holds for both cases, with a slightly different definition of the depletion layer capacitance, $C_{dep} = \epsilon A_0 / (d + x_n)$.

There are three mechanisms that contribute to the change in x_n . The first is the current flowing in the external circuit, which pushes the electron cloud forward and thus decreases the width of the depletion layer. The second is the forward injection of electrons into the active layer across the depletion layer. This forward-injection mechanism increases the space charge at both sides of the depletion layer and increases the depletion layer width x_n . The third is the backward injection of electrons from the active region back to the n-type layer across the depletion layer, which decreases the depletion layer width x_n .

7.2.2 Semiclassical Langevin Equation for Junction Voltage Dynamics

The forward-injection mechanism is modeled as diffusion of electrons across the depletion layer from the n-type layer to the p-type layer. The average forward-injection diffusion current is given by $I_{fi} = \frac{1}{2} e n_p v A_0$, where n_p is the electron density at $x = 0$ and v is thermal velocity of the electron in the $-x$ direction, given by l_f / τ_f [11]. Here, l_f is the electron mean-free-path and τ_f is the mean-free-time. Using $n_p = n_{p0} \exp[eV_j / k_B T]$ and the Einstein relation $D_n = l_f^2 / 2\tau_f$, where n_{p0} is the equilibrium electron concentration in the p-type layer and D_n is the electron diffusion constant, one gets[6]

$$I_{fi}(t) = \frac{q n_{p0} D_n A_0}{l_f} \exp\left(\frac{q V_j(t)}{k_B T}\right) \quad . \quad (7.30)$$

The minority carrier distribution for $x < 0$, in the presence of radiative recombination with carrier lifetime of τ_{sp} , is given by $n_p(x) = n_{p0} + (n_p - n_{p0}) \exp(x/L_n)$ with $L_n^2 = D_n \tau_{sp}$. The total number of excess electrons in the active region is given by integrating $n_p(x) - n_{p0}$ from $x = -\infty$ to $x = 0$

$$N = A_0 L_n (n_p - n_{p0}) \quad . \quad (7.31)$$

Since the thermal motion is random, there are carriers that are injected back from the active region into the n-type layer. On average, this backward-injection current is proportional to the carrier flux in the $+x$ direction from $x = -l_f$,

$$I_{bi}(t) = \frac{qD_n A_0}{l_f} \left(n_{p0} + \frac{N}{A_0 L_n} \exp(-l_f/L_n) \right) . \quad (7.32)$$

The net diffusion current I is given by the difference between the forward- and backward-injection currents. Expanding $\exp(-l_f/L_n) \simeq 1 - l_f/L_n$ yields

$$I = \frac{qD_n A_0}{L_n} n_{p0} [\exp(qV_j/k_B T) - 1] = I_0 [\exp(qV_j/k_B T) - 1] , \quad (7.33)$$

where $I_0 = eD_n A_0 n_{p0}/L_n$ is the reverse saturation current.

Since the forward- and backward-injection currents change the depletion layer width, they will affect the junction voltage according to Eq. (7.26) or Eq. (7.29). After taking the effects of these currents into account, Eq. (7.25) reduces to

$$\frac{dV_j}{dt} = \frac{1}{C_{dep}} I_{ext}(t) - \frac{1}{C_{dep}} I_{fi}(t) + \frac{1}{C_{dep}} I_{bi}(t) . \quad (7.34)$$

Let us consider the diffusion (or thermionic emission) of an electron across the depletion layer as a discrete and instantaneous process. Imagine a forward-injection event occurring at time $t = t_0$. The junction voltage drop due to the forward-injection process is $\Delta V_j = e/C_{dep}$. This will, on average, decrease the forward-injection current by a factor

$$\begin{aligned} \frac{I_{fi}(t = t_0+)}{I_{fi}(t = t_0-)} &= \frac{I_0 \exp[eV_j(t = t_0+)/k_B T]}{I_0 \exp[eV_j(t = t_0-)k_B T]} \\ &= \exp\left(-\frac{q}{k_B T} \Delta V_j\right) \\ &\equiv \exp(-r) , \end{aligned} \quad (7.35)$$

where $r \equiv \left(\frac{e^2}{C_{dep}}\right)/k_B T$, the ratio between the single-electron charging energy and thermal energy. It should be noted that this is a comparison of the single-electron charging energy e^2/C_{dep} with the characteristic energy scale to change the forward-injection current significantly, which for the case of a pn junction happens to coincide with the thermal energy, $k_B T$.

For a normal laser diode or LED with a large capacitance, C_{dep} , operating at reasonably high temperature (≥ 4 K), the factor r is much smaller than unity. Under this condition, a single carrier-injection event does not change the average forward-injection current appreciably. In this limit, one can split the forward-injection current into two parts: an average current which varies only as a function of the time-dependent junction voltage and a stochastic noise current due to individual random injection events which have zero average. The forward-injection current term can be written as

$$I_{fi}(t) = \frac{qD_n A_0}{l_f} \exp\left(\frac{qV_j(t)}{k_B T}\right) + q F_{fi} , \quad (7.36)$$

where $V_j(t)$ denotes a time-dependent junction voltage and F_{fi} is the Langevin noise term. Since F_{fi} arises from collisions with a reservoir of phonons and other electrons which have large degrees of freedom, the correlation time is infinitesimally short. Therefore, one obtains the Markovian correlation function

$$\langle F_{fi}(t)F_{fi}(t') \rangle = \frac{2\langle I_{fi}(t) \rangle}{q} \delta(t - t') \quad , \quad (7.37)$$

where $\langle I_{fi}(t) \rangle$ denotes the slowly varying average forward-injection current. One can make similar arguments for the backward-injection current, and thus obtain

$$I_{bi}(t) = \frac{qD_n A_0}{l_f} \left(n_{p0} + \frac{N}{A_0 L_n} \exp(-l_f/L_n) \right) + q F_{bi} \quad , \quad (7.38)$$

with

$$\langle F_{bi}(t)F_{bi}(t') \rangle = \frac{2\langle I_{bi}(t) \rangle}{q} \delta(t - t') \quad . \quad (7.39)$$

To describe the effect of different driving conditions, consider the case where the *pn* junction is connected to a constant voltage source, with a series resistor, R_s , that carries thermal voltage noise, V_s (Fig. 7.7(a)). The forward- and backward-injection events are described in the equivalent circuit model (Fig. 7.7(b)) as independent current sources (I_{fi} and I_{bi}) charging or discharging the depletion layer capacitor C_{dep} . Defining $F_{rs} \equiv V_s/eR_s$, the external current is given by

$$I_{ext}(t) = \frac{V - V_j}{R_s} + q F_{rs} \quad , \quad (7.40)$$

with

$$\langle F_{rs}(t)F_{rs}(t') \rangle = \frac{4k_B T}{q^2 R_s} \delta(t - t') \quad , \quad (7.41)$$

and Eq. (7.34) is reduced to

$$\frac{dV_j}{dt} = \frac{V - V_j}{R_s C_{dep}} - \frac{I_{fi}(V_j)}{C_{dep}} + \frac{I_{bi}(N)}{C_{dep}} + \frac{q}{C_{dep}} (-F_{fi} + F_{bi} + F_{rs}) \quad . \quad (7.42)$$

7.2.3 Semiclassical Langevin Equation for Electron Number and Photon Flux

In this section, the semi-classical Langevin equations that describe the noise properties of an LED are introduced. The carriers are injected into the active layer, and the junction voltage fluctuation is described by Eq. (7.42). The total number of electrons N in the active p-type layer increases by forward-injection current and photon absorption, and it decreases due to backward-injection current and radiative recombination. The absorption and radiative recombination are described by a Poisson point process with a fixed lifetime of τ_{sp} . Optical losses (either internal or external) are modeled as a beam splitter with transmission probability η ($0 \leq \eta \leq 1$). The equations that describe the system are

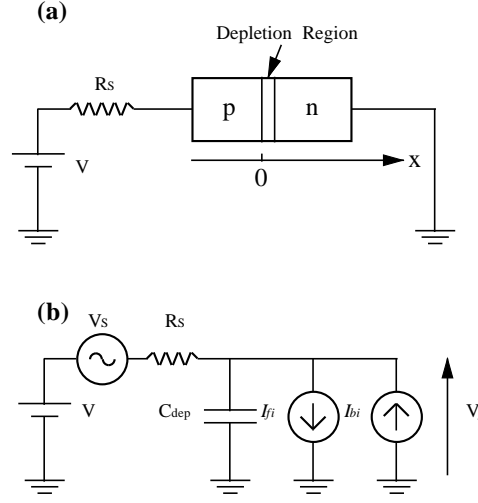


Figure 7.7: (a) A pn junction diode connected in series with a resistor R_s that carries voltage noise of V_s , altogether biased by a constant-voltage source, V . (b) Equivalent circuit model

$$\frac{C_{dep}}{q} \frac{dV_j}{dt} = \frac{V - V_j}{qR_s} - \frac{I_{fi}(V_j)}{q} + \frac{I_{bi}(N)}{q} - F_{fi} + F_{bi} + F_{rs} \quad , \quad (7.43)$$

$$\frac{dN}{dt} = -\frac{N + N_{p0}}{\tau_{sp}} + \frac{N_{p0}}{\tau_{sp}} + \frac{I_{fi}(V_j)}{q} - \frac{I_{bi}(N)}{q} - F_{sp} + F_{fi} - F_{bi} \quad , \quad (7.44)$$

$$\Phi = \eta \left[\frac{N + N_{p0}}{\tau_{sp}} - \frac{N_{p0}}{\tau_{sp}} + F_{sp} \right] + F_v \quad . \quad (7.45)$$

$N_{p0}/\tau_{sp} = n_{p0}A_0L_n/\tau_{sp} = I_0/q$ gives the rate of absorption and recombination for background electron concentration in the active region. F_{sp} is the noise term corresponding to absorption and radiative recombination. Since these processes arise from coupling with thermal photon field reservoirs, the correlation of F_{sp} becomes

$$\langle F_{sp}(t)F_{sp}(t') \rangle = 2 \frac{N + 2N_{p0}}{\tau_{sp}} \delta(t - t') \quad . \quad (7.46)$$

The noise source corresponding to forward injection, F_{fi} , appears in the equations for both the carrier number Eq. (7.44) and the junction voltage Eq. (7.43) and the two terms are negatively correlated. The same is true for F_{bi} . Φ is the photon flux measured at the photodetector, after the photons pass through a beam splitter of transmission probability η . The beam splitter introduces partition noise, F_v , which has a Markovian correlation of

$$\langle F_v(t)F_v(t') \rangle = 2\eta(1 - \eta) \frac{N + 2N_{p0}}{\tau_{sp}} \delta(t - t') \quad , \quad (7.47)$$

since the noise comes from the vacuum fluctuations coupled in from the open port of the beam splitter.

A. Steady-State Conditions

In the steady state, Eqs. (7.44) and (7.43) yield

$$\frac{N_0}{\tau_{sp}} = \frac{I_{fi}(V_0)}{q} - \frac{I_{bi}(N_0)}{q} = \frac{V - V_0}{qR_s}, \quad (7.48)$$

where the subscript “0” denotes the steady-state values. If the dc current $I \equiv (V - V_0)/(eR_s)$ is given, Eq. (7.48) can be used to determine the following quantities:

- $N_0 = \frac{V - V_0}{eR_s} \tau_{sp}$,
- $\Phi_0 = \eta \frac{N_0}{\tau_{sp}}$,
- $I_{bi}(N_0)$ (Eq. (7.38)),
- $I_{fi}(V_0) = I + I_{bi}(N_0)$,
- $I_{fi}(V_0) - I_{bi}(N_0) = \frac{V - V_0}{qR_s}$ determines $I_{fi}(V_0)$ and thus V_0 .

B. Linearization

Once the steady-state conditions are determined, one can linearize the equations around these steady-state values

$$N = N_0 + \Delta N, \quad (7.49)$$

$$V_j = V_0 + \Delta V, \quad (7.50)$$

$$\Phi = \Phi_0 + \Delta \Phi. \quad (7.51)$$

We now introduce the forward and backward emission times defined by

$$\frac{1}{\tau_{fi}} = \frac{1}{C_{dep}} \frac{d}{dV_j} I_{fi}(V_j) \Big|_{V_j=V_0} = \frac{qI_{fi}(V_0)}{k_B T C_{dep}}, \quad (7.52)$$

$$\frac{1}{\tau_{bi}} = \frac{1}{q} \frac{d}{dN} I_{bi}(N) \Big|_{N=N_0} = \frac{I_{bi}(N_0)}{q[N_0 + n_{p0} A_0 L_n \exp(l_f/L_n)]}. \quad (7.53)$$

Since the electron mean-free-path l_f is much smaller than the electron diffusion length L_n , at reasonably high bias, $qV_j/k_B T \gg 1$, the relation

$$I_{fi}(V_0) \simeq I_{bi}(N_0) \gg I \quad (7.54)$$

is obtained, with $I = I_{fi}(V_0) - I_{bi}(N_0)$, where $I_{fi}(V_0)$ and $I_{bi}(N_0)$ are the average forward- and backward-injection currents, respectively. The time constants τ_{fi} and τ_{bi} represent the characteristic time scales of thermal fluctuations. These are the shortest time scales in the problem.

C. Photon-Flux Noise

The ‘‘thermionic emission time’’, τ_{te} , satisfies

$$\tau_{te} \equiv R_d C_{dep} = \frac{k_B T C_{dep}}{q(I + I_0)} \simeq \tau_{fi} \tau_{sp} / \tau_{bi} \quad . \quad (7.55)$$

The last equality follows from $I = I_{fi}(V_0) - I_{bi}(N_0)$ and Eqs. (7.48), (7.52) and (7.53). τ_{te} is the time scale over which V_j fluctuates by $k_B T / q$. Using this definition, the photon flux spectrum is obtained as:

$$S_{\Delta\Phi} = \eta \frac{2I}{q} (1 - \eta \chi(\Omega)) + \eta \frac{4k_B T}{q^2 R_{d0}} \left[1 - \eta \chi(\Omega) \left(1 + \frac{\tau_{te}}{\tau_{RC}} \right) \right] \quad , \quad (7.56)$$

where $R_{d0} = (dV_j/dI)|_{V_j=0}$ is the differential resistance of the junction at zero bias, and

$$\chi(\Omega) \simeq \left[\left(1 + \frac{\tau_{te}}{\tau_{RC}} \right)^2 + \Omega^2 (\tau_{sp} + \tau_{te})^2 \right]^{-1} \quad . \quad (7.57)$$

When the junction is driven by a constant-current source, the condition $\tau_{RC} \gg \tau_{sp}, \tau_{te}$ is satisfied. In this case, Eq. (7.56) is further reduced to

$$S_{\Delta\Phi} \rightarrow \eta \left(\frac{2I}{q} + \frac{4k_B T}{q^2 R_{d0}} \right) \left(1 - \frac{\eta}{1 + \Omega^2 (\tau_{sp} + \tau_{te})^2} \right) \quad . \quad (7.58)$$

The photon-flux noise is reduced to below the shot-noise value at frequencies lower than $1/(\tau_{sp} + \tau_{te})$. At very low frequencies, the normalized photon flux noise $S_{\Delta\Phi} \cdot q/2\eta I$ is $1 - \eta$. At high frequencies, it approaches the full shot-noise value. This is in agreement with experimental observation[12].

When the junction is driven by a constant voltage source, $\tau_{RC} \ll \tau_{sp}, \tau_{te}$, we have

$$S_{\Delta\Phi} \rightarrow \eta \left(\frac{2I}{e} + \frac{4k_B T}{e^2 R_{d0}} \right) \quad . \quad (7.59)$$

In this case, the photon flux noise is full shot noise limited at all frequencies at high bias ($I \gg I_0$).

Figure 7.8(a) shows the normalized photon flux noise power spectral density Eq. (7.56) of an LED under high bias ($I \gg I_0$). The junction parameters, like the depletion layer capacitance C_{dep} and temperature θ , are fixed and the current is adjusted so that $\tau_{te} = \tau_{sp}$. One can see that as the source resistance R_s (and thus the time constant of the circuit τ_{RC}) is increased, the noise at low frequencies is reduced to below the Poisson limit. The effect of finite quantum efficiency ($\eta = 0.5$) is shown in Fig. 7.8(b). The ultimate intensity squeezing level is determined by the imperfect quantum efficiency.

One can define the squeezing bandwidth to be the frequency at which the degree of squeezing is reduced by a factor of 2 compared to the squeezing at zero frequency. This can be explicitly calculated from Eq. (7.58)

$$f_{3dB} = \frac{1}{2\pi(\tau_{sp} + \tau_{te})} \quad . \quad (7.60)$$

In Fig. 7.9, the noise power spectral density under different driving currents is plotted, and the dependence of squeezing bandwidth on current is shown. It should be noted that

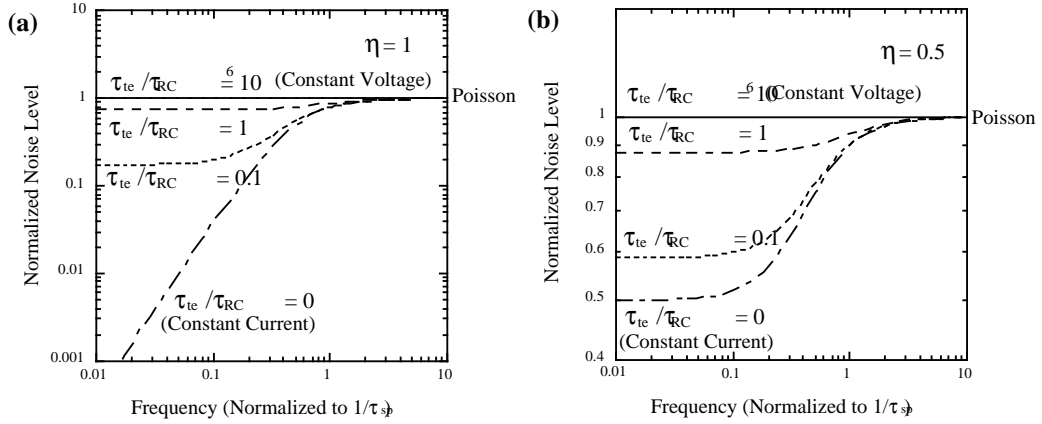


Figure 7.8: LED noise power spectral density calculated for a junction under different bias conditions, at high bias ($I \gg I_0$). Operation current is chosen so that $\tau_{te} = \tau_{sp}$. The bias condition is treated by changing the series resistor R_s , and thus the time constant τ_{RC} . (a) Unity quantum efficiency ($\eta = 1$); (b) $\eta = 0.5$

the squeezing bandwidth is affected neither by the value of source resistance nor by the quantum efficiency.

D. Noise in the External Circuit Current

The linearized Langevin equations allow us to calculate the power spectrum of the external circuit current. The external current noise spectral density approaches the thermal noise $4k_B T/R_s$ with a constant-current source ($\tau_{RC} \gg \tau_{sp}, \tau_{te}$). With a constant-voltage source ($\tau_{RC} \ll \tau_{sp}, \tau_{te}$), the noise approaches $2eI + 4k_B T/R_{d0}$.

Figure 7.10 shows the schematic dynamics of a stochastic photon emission event, the junction voltage fluctuation, and the relaxation current in the external circuit. The correlation between the junction voltage and carrier number in the active region is perfect for macroscopic pn junctions in the diffusion limit. A photon emission event accompanies a reduction in the carrier number, which creates a junction voltage drop of q/C_{dep} . This fluctuation in the voltage is recovered by a relaxation current flow in the external circuit with a time scale of τ_{RC} . When the junction is driven with a constant-voltage source (Fig. 7.10(a)), the junction voltage (and thus the carrier number) recovers very quickly, and the next emission event is independent of the previous event. The photon-emission event is a Poisson point process, and the relaxation current flows accordingly. The external current therefore features the full shot noise. In the constant-current-driven case (Fig. 7.10(b)), the relaxation current flows very slowly; thus, the next photon-emission event occurs before the external circuit completely recovers the junction voltage. The external circuit current due to the second emission event is superimposed on the first one, and the resulting fluctuation is less than the shot noise.

The carriers jump back and forth across the depletion layer and establish the correla-

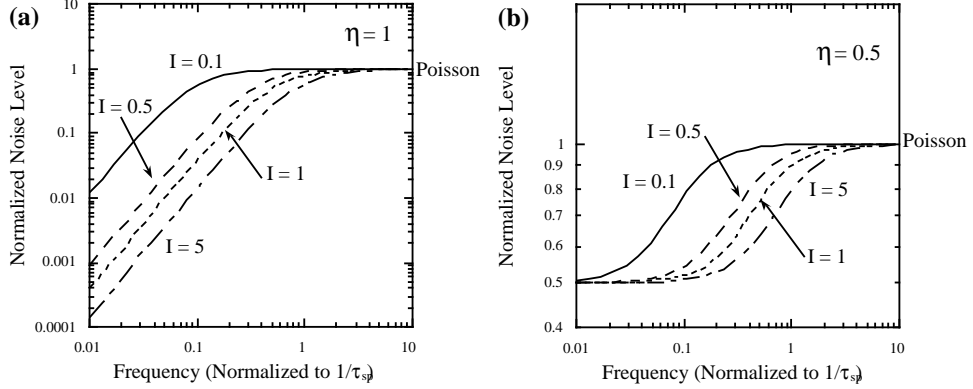


Figure 7.9: LED noise power spectral density calculated for a junction driven by a constant current source, at high bias ($I \gg I_0$). Frequency is normalized to $1/\tau_{sp}$ and current is normalized to $I_N = \frac{e}{r\tau_{sp}}$, so that $I = I_N$ corresponds to $\tau_{te} = \tau_{sp}$. **(a)** Unity quantum efficiency ($\eta = 1$); **(b)** $\eta = 0.5$

tion between the junction voltage and the carrier number. However, these events do not contribute to the external current noise, because the effective resistance across the junction depletion layer ($k_B T/qI_{fi}$, $k_B T/qI_{bi}$) is so small that the junction voltage drop induced by a forward- (backward-) injection event will be relaxed mostly by a direct backward- (forward-) injection event rather than through the external circuit. This means that the forward- and backward- injection events will not be seen from the external circuit and all the noise will come from the recombination event in the active region.

E. Correlation Between Carrier Number and Junction Voltage

The normalized correlation between the junction voltage fluctuation and the carrier number fluctuation is defined as

$$C_{n,v}(\Omega) \equiv \frac{\langle \frac{C_{dep}}{q} \Delta \tilde{N}^*(\Omega) \Delta \tilde{V}_j(\Omega) \rangle}{\langle \Delta \tilde{N}^*(\Omega) \Delta \tilde{N}(\Omega) \rangle^{\frac{1}{2}} \langle \frac{C_{dep}}{q} \Delta \tilde{V}_j^*(\Omega) \frac{C_{dep}}{q} \Delta \tilde{V}_j(\Omega) \rangle^{\frac{1}{2}}} \quad (7.61)$$

where * denotes the complex conjugate. One can calculate the correlation $|C_{v,n}|$ from the linearized Langevin equations.

$|C_{v,n}|$ approaches 1 and there is a perfect correlation between the junction voltage and the carrier number in the active region no matter what the driving condition is (i.e., for all values of τ_{RC}). The physical reason behind this is the fast (forward- and backward-) injection events which quickly restore a unique relation between carrier number fluctuation and junction voltage fluctuation with the characteristic relaxation time $\sim \tau_{fi}, \tau_{bi}$. Since this relaxation is so fast, fluctuation of one of the two variables will immediately be followed by fluctuation of the other.

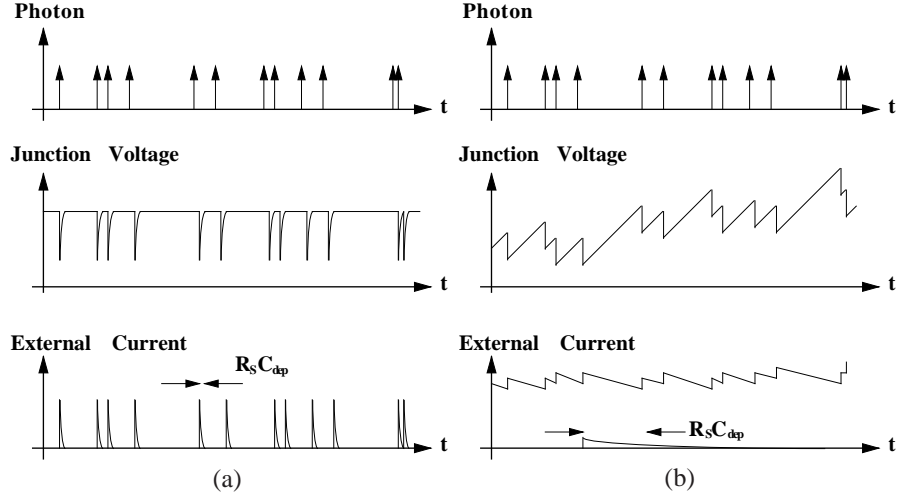


Figure 7.10: Schematic showing the photon emission, junction voltage dynamics, and external current flow of a pn junction. (a) Constant-voltage-driven case; (b) constant-current-driven case

F. Correlation Between Photon Flux and Junction Voltage

The normalized correlation between the photon flux and junction voltage fluctuation is defined as

$$C_{\Phi,v}(\Omega) \equiv \frac{\langle \Delta \tilde{\Phi}^*(\Omega) \frac{C_{dep}}{q} \Delta \tilde{V}_j(\Omega) \rangle}{\langle \Delta \tilde{\Phi}^*(\Omega) \Delta \tilde{\Phi}(\Omega) \rangle^{\frac{1}{2}} \langle \frac{C_{dep}}{q} \Delta \tilde{V}_j^*(\Omega) \frac{C_{dep}}{q} \Delta \tilde{V}_j(\Omega) \rangle^{\frac{1}{2}}}, \quad (7.62)$$

which one can calculate similarly using the linearized Langevin equations:

$$|C_{\Phi,v}(\Omega)|^2 \simeq \frac{(\tau_{te}/\tau_{RC})^2 + \Omega^2(\tau_{sp} + \tau_{te})^2}{(1 + 2\tau_{te}/\tau_{RC}) \left\{ \frac{1}{\eta} [(1 + \tau_{te}/\tau_{RC})^2 + \Omega^2(\tau_{sp} + \tau_{te})^2] - 1 \right\}}. \quad (7.63)$$

When the junction is driven with a constant-voltage source, this correlation reduces to 0, because the junction voltage fluctuation is merely determined by the noise in the external resistor. When the junction is driven with a constant-current source, the correlation reduces to

$$|C_{\Phi,v}(\Omega)|^2 \rightarrow \frac{\Omega^2(\tau_{sp} + \tau_{te})^2}{\frac{1}{\eta} [1 + \Omega^2(\tau_{sp} + \tau_{te})^2] - 1}. \quad (7.64)$$

Whenever the photon is emitted, the junction voltage drops by q/C_{dep} , but it takes a long time for the external circuit to recover the junction voltage. If the photon is lost

due to finite quantum efficiency, the junction voltage will decrease without a photon being detected, resulting in a decrease in correlation. This results in a correlation of η at high frequencies [compared to $1/(\tau_{sp} + \tau_{te})$]. As the observation time gets longer (at lower frequencies), a second photon can be emitted after $\sim \tau_{sp}$ or the junction voltage will fluctuate by approximately $k_B T/q$ over time $\sim \tau_{te}$. This results in the loss of correlation at lower frequencies. This is illustrated in Fig. 7.11, where the correlation is shown for several values of η .

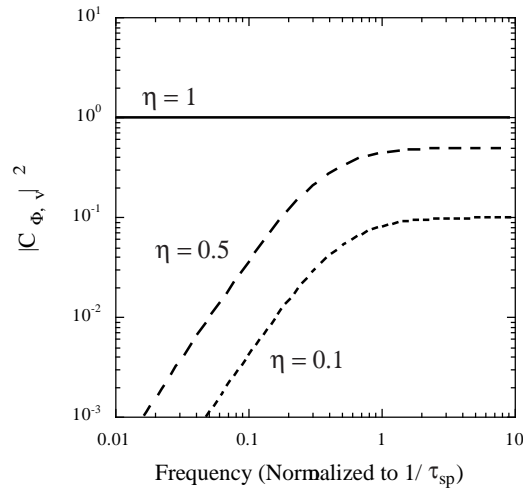


Figure 7.11: Normalized correlation $|C_{\Phi, v}|^2$ for several values of η when the LED is driven with a constant-current source

7.3 Experimental Evidence for Intensity Squeezing and Quantum Correlation

7.3.1 Intensity Squeezing due to Macroscopic Coulomb Blockade Effect in LED's

The suppression of noise in the external circuit current does not guarantee regulated carrier-injection into an active layer across a depletion layer potential barrier. This is because the individual carrier injection is a random process, only the average rate of which is determined by the junction voltage and the temperature of the junction. However, as discussed in the previous section, when a carrier is injected, the space charge in the depletion layer capacitance increases by q , and this decreases the junction voltage by q/C_{dep} . This decrease in the junction voltage decreases the carrier-injection rate, establishing a negative feedback mechanism to suppress the noise in the carrier-injection process. If the junction (depletion layer) capacitance, C_{dep} , is large and the operation temperature, θ , is high, the junction voltage drop, q/C_{dep} , due to a single carrier-injection event is much smaller than the thermal fluctuation voltage, $k_B T/q$, so that the individual carrier-injection event

does not influence the following event. We have a completely random point process with a constant rate in such a macroscopic pn junction at a high temperature, even though the junction is driven by a “perfect constant-current source”[1].

Even in the macroscopic, high-temperature limit, the collective behavior of many electrons charging the depletion layer capacitance, C_{dep} , can amount to establishing regularity in the carrier-injection process. A single electron injection event reduces the junction voltage by q/C_{dep} , so the successive injection of $N = \left(\frac{k_B T}{q}\right) / \left(\frac{q}{C_{dep}}\right) = k_B T C_{dep} / q^2$ electrons reduces the junction voltage by the thermal voltage $k_B T / q$. Such a change in the junction voltage can result in significant modification of the carrier-injection rate. Since carriers are provided by the external circuit at a rate of I/q , the time necessary for N carriers to be supplied can be calculated as

$$\tau_{te} = \frac{k_B \theta C_{dep}}{qI} = N\tau \quad , \quad (7.65)$$

where $\tau = \frac{q}{I}$ is the single-electron charging time. This time-scale is named “thermionic emission time”, and is identical to Eq. (7.55) in the high-current limit ($I \gg I_0$). The junction current follows $\sim \exp(eV_j/k_B\theta)$, where V_j is the junction voltage. Therefore, τ_{te} is the time scale over which the junction current changes significantly. A carrier-injection event is completely stochastic at the microscopic level, but the junction voltage modulation induced by many ($\sim N$) carriers collectively regulates a global carrier-injection process over the time scale τ_{te} . If the measurement time, T_{meas} , is much longer than τ_{te} , the electron-injection process becomes sub-Poissonian. This is because the continuous charging or successive injection of N electrons modulates the junction voltage greater than $k_B T / q$, and, therefore, influences the subsequent events. If the measurement time, T_{meas} , is longer than τ_{te} , the variance of the injected electrons is given by the following fundamental limit[1]:

$$\langle \Delta n_e^2 \rangle = \frac{k_B \theta C_{dep}}{q^2} = N \quad . \quad (7.66)$$

This variance is independent of the measurement time, T_{meas} , and the average electron number, $\langle n_e \rangle = \frac{I}{q} T_{meas}$. This independence is at the heart of squeezed light generation by a constant-current-driven pn junction: as the measurement time becomes longer, so does the degree of squeezing which is measured as $\langle \Delta n_e^2 \rangle / \langle n_e \rangle$. For a typical LED operating at room temperature, this fundamental noise limit $\langle \Delta n_e^2 \rangle$ is on the order of $10^7 \sim 10^8$. This fundamental limit of intensity noise squeezing manifests itself by a finite squeezing bandwidth given by[1]

$$B = \frac{1}{2\pi\tau_{te}} = \frac{qI}{2\pi k_B \theta C_{dep}} \quad . \quad (7.67)$$

There is another source of stochasticity in addition to thermionic emission or tunneling of carriers in a constant-current-driven LED, which is the radiative recombination of the injected carriers. When this is taken into account, the squeezing bandwidth over which the intensity noise is reduced to below the shot-noise value is given by:

$$f_{3dB} = \frac{1}{2\pi(\tau_{te} + \tau_{sp})} = \frac{1}{2\pi\left(\frac{k_B \theta C_{dep}}{qI} + \tau_{sp}\right)} \quad , \quad (7.68)$$

where τ_{sp} is the radiative lifetime. Therefore, the squeezing bandwidth should be proportional to the current, I , and inversely proportional to the temperature, θ , and the capacitance, C_{dep} , in a low-current regime, but is limited by the radiative recombination lifetime in a high-current regime.

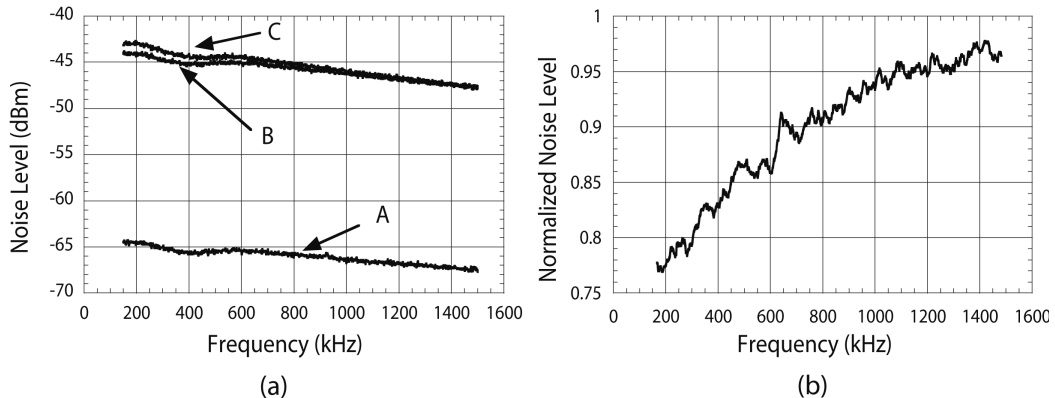


Figure 7.12: A typical set of noise measurement data. The photocurrent was 4.73 mA, and the temperature was 295 K. (a) The noise spectra measured by the spectrum analyzer. Trace A is the thermal background noise, trace B is the photocurrent noise when the LED was driven with a constant-current source, and trace C is the photocurrent noise when the LED was driven with a shot-noise-limited current source. (b) The intensity noise of the constant-current-driven LED normalized by the shot-noise value. The thermal background noise was subtracted from both traces B and C before normalization

Figure 7.12 shows a typical set of noise measurement data for a GaAs LED driven by a constant current source[12]. Traces A, B and C in Fig. 7.12(a) show the thermal background noise, the photocurrent noise when the LED was driven with a high-impedance constant-current source, and the photocurrent noise when the LED was driven with a shot-noise-limited current source, respectively. The shot noise limited current source is obtained by a reverse-biased pn junction photodiode illuminated by highly attenuated LED light[12]. The photocurrent noise was about 20 dB above the thermal noise, and the detector response was reasonably flat in the frequency region of interest. One can see that the photocurrent noise for a constant-current-driven LED is below the shot-noise value in the low-frequency regime, but it approaches the shot-noise value in the higher-frequency regime. The thermal noise trace (A) was subtracted from the two photocurrent noise traces (B and C), and the squeezed noise trace (B) was normalized by the shot-noise-limited trace (C). Figure 7.12(b) shows such a normalized noise spectrum. The maximum squeezing observed in the low-frequency region is about 0.21 (1.0 dB), which is in good agreement with the expected value from the overall quantum efficiency. The squeezing bandwidth was determined to be the frequency at which the degree of squeezing is reduced by a factor of two and was found to be ~ 720 kHz in this specific case.

Figure 7.13(a)–(d) shows the squeezing bandwidth of four LEDs with different deple-

tion layer capacitances at room temperature. The dotted lines are the expected squeezing bandwidths due to macroscopic Coulomb blockade effect Eq. (7.67). The dashed lines show the lifetime limitation of the squeezing bandwidth, with $\tau_{rad} = 290$ ns and the corresponding bandwidth of 560 kHz. The solid lines show the theoretical squeezing bandwidth including the two effects Eq. (7.68). In a low-current regime, the squeezing bandwidth increases linearly with increasing the current. The four capacitance values used to fit the measurement curves were 6.5 nF, 30 nF, 90 nF and 180 nF. The ratios of these four capacitance values are 0.072 : 0.33 : 1.0 : 2.0. They are in close agreement with the ratios of the junction areas, 0.073 : 0.42 : 1.0 : 2.1.

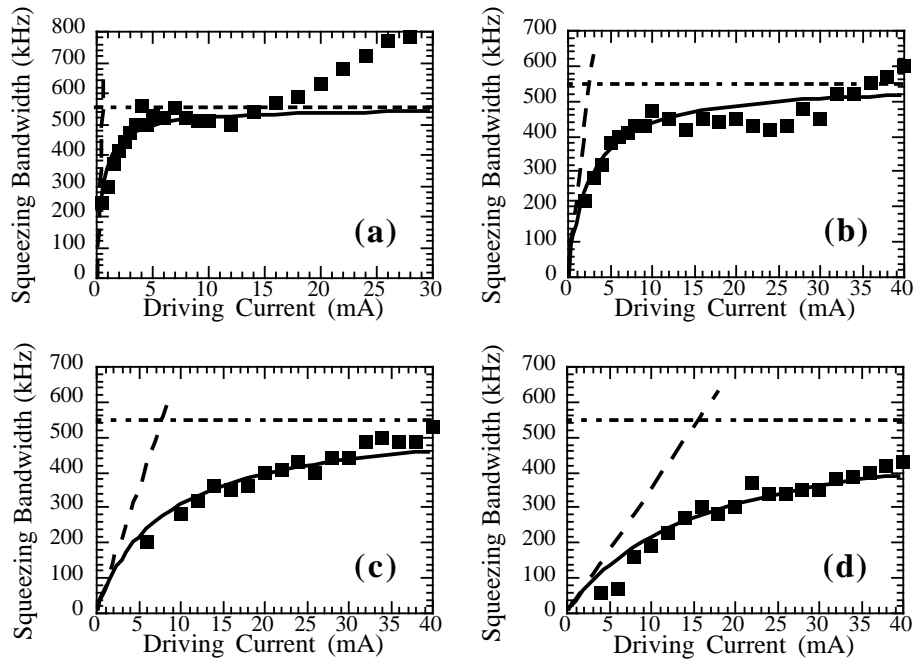


Figure 7.13: The squeezing bandwidth as a function of a driving current for various LEDs at room temperature. *Dashed lines* show the radiative recombination lifetime limitation of about 560 kHz (carrier lifetime of 290 ns). *Dotted lines* are the squeezing bandwidths expected from (3.3). *Solid lines* are the expected overall squeezing bandwidth expressed by (3.4). Areas of the LEDs (capacitance values to fit the data) are (a) 0.073 mm^2 (6.5 nF), (b) 0.423 mm^2 (30 nF), (c) 1.00 mm^2 (90 nF) and (d) 2.10 mm^2 (180 nF)

As the driving current increases, the squeezing bandwidth is limited by the carrier recombination lifetime and saturates at ~ 560 kHz. For the smallest-area LED, the squeezing bandwidth increases above this value at higher driving currents. This is attributed to the carrier-concentration-dependent radiative lifetime. At higher current densities, the carrier density in the active region increases, and the carrier lifetime is shortened. This results in the increased squeezing bandwidth.

Figure 7.14(a)–(d) shows the squeezing bandwidth of the LED with an area of 1.00

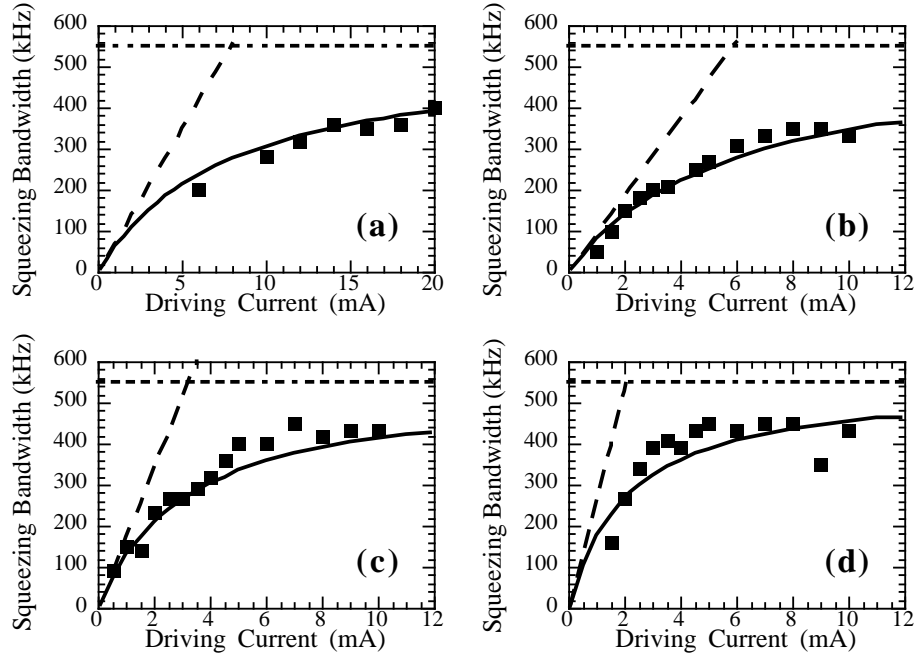


Figure 7.14: The squeezing bandwidth as a function of driving current for various temperatures. The area of the LED was 1.00 mm^2 . The temperatures are (a) 295 K (identical to Fig. 3.4c), (b) 220 K, (c) 120 K and (d) 78 K. *Dashed lines* show the radiative recombination lifetime limitation of about 560 kHz. *Dotted lines* are squeezing bandwidths expected from (3.3). *Solid lines* are the overall bandwidths expected from (3.4). A junction capacitance of 90 nF and a carrier lifetime of 290 ns obtained by room-temperature measurement (Fig. 7.13) were used

mm^2 measured at different temperatures. The squeezing bandwidth was measured at 295 K, 220 K, 120 K and 78 K. Again, the dotted lines show the squeezing bandwidth limitation due to the macroscopic Coulomb blockade effect, and the dashed lines show the limitation due to the recombination lifetime at ~ 560 kHz. The solid lines are the theoretical squeezing bandwidth limitation including both effects Eq. (7.68). There are no fitting parameters in the curves, except for the capacitance $C_{dep} = 90 \text{ nF}$ obtained by fitting the data in Fig. 7.13(c). Actual temperatures at which the measurements were made were used to draw the curves. From this data, one can see that the squeezing bandwidth is linearly proportional to the driving current in the low-current regime and saturates at the radiative lifetime limited value of ~ 560 kHz in the high-current regime. The linear slope in the low-current regime is inversely proportional to temperature. Close agreement between the experimental result and the simple theoretical model described by Eq. (7.68) can be seen.

7.3.2 Quantum Correlation between the Junction-Voltage Fluctuation and the Intensity Fluctuation in a Semiconductor Laser

A laser oscillator is an open quantum system where the mean values and variances in the system observables are established by a balance of the ordering force of the system and the fluctuating forces from the reservoirs. It has been well established that a beam with sub-Poissonian photon-number fluctuation can be generated directly from a pump-number fluctuation can be generated directly from a pump-noise-suppressed semiconductor laser[13],[14]. This is a complex problem, the details of which we will study in chapter 12.

In such a constant-current-driven semiconductor laser, the junction voltage is free to fluctuate. The junction-voltage fluctuation is uniquely related to the electron-number fluctuation $\Delta\hat{N}_c$ through the junction capacitance, $\hat{v}_n = q\Delta\hat{N}_c/C$. The electron-number fluctuation is toggled by spontaneous emission, stimulated emission, and absorption processes. If the electron system is predominantly coupled to a single lasing mode and also if the output coupling rate is much higher than the internal photon loss rate, the correlation between the junction-voltage fluctuation and the output intensity (photon-number) fluctuation is perfect and negative. This is because if the electron number decreases by 1, then the photon number of the output field must increase by 1. In a real semiconductor laser, however, the spontaneous emission occurs into non-lasing modes and internal photon loss rate cannot be neglected. Whether the correlation may extend into the quantum domain or not is not clear by a simple intuitive argument.

The theoretical and experimental results[8] demonstrate that the correlation penetrates into the quantum regime. The experimental arrangement is shown in Fig. 7.15. Two photo detectors were arranged in a balanced configuration. A semirigid coaxial cable provided a delay T_d for the photocurrent noise. The junction voltage measured by amplifier A2 was subtracted from the amplified photocurrent at a wideband 180° hybrid.

Figure 7.16 shows the measured junction-voltage noise (trace *a*), the semiconductor laser intensity noise (trace *b*), and the shot noise produced by the LED (trace *c*). Trace *d* is the spectral density of the combined signal, $v_n(\Omega) - g_r\Delta r(\Omega)e^{i\Omega T_d}$, where g_r is a relative-gain parameter. $v_n(\Omega)$ and $\Delta r(\Omega)$ are the Fourier component of the junction voltage and intensity fluctuations. The laser bias level was $r \equiv I/I_{th} - 1 = 9.7$.

The sinusoidal variation shown by trace *d* in Fig. 7.16 indicates a correlation between the intensity (photon-number) fluctuation and the junction-voltage fluctuation. In the absence of a correlation, trace *d* would be flat and the noise power numerically equal to the sum of the noise powers given by traces *a* and *b*. Separate measurement of the spectral densities of the sum and difference of the amplitudes, $S_{v_n \pm g_r \Delta r} = \langle (v_n \pm g_r \Delta r)^2 \rangle$, taken from the respective ports of the hybrid tee—with the delay line absent—confirms that the correlation is *negative*. That is, the spectral density of the difference signal $S_{v_n - g_r \Delta r}$ is larger than the sum. The fact that the minimum of the signal in trace *d* ($S_{v_n + g_r \Delta r}$) is below $\langle v_n^2 \rangle + g_r^2 \langle (\Delta r)^2 \rangle$ is indicative of a quantum correlation, because the laser amplitude noise is already below the standard shot noise level. The measured correlation $C_{vr} = -0.40 \pm 0.02$ can be compared with a theoretical estimate of -0.38 [8].

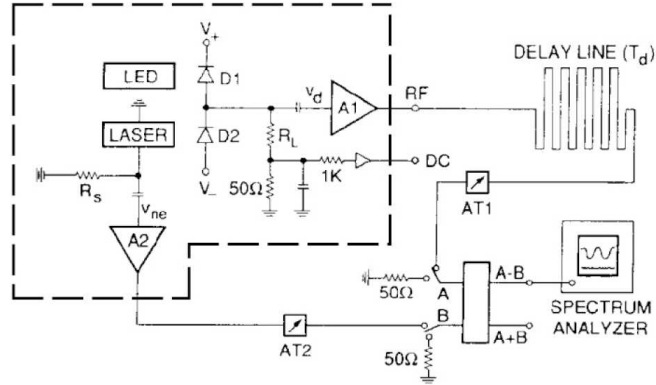


Figure 7.15: Basic experimental arrangement. The apparatus inside the dotted lines was enclosed in a closed-cycle refrigerator and the temperature was maintained at 66 K. Photocurrent noise v_{ne} and the junction-voltage noise v_d are combined using a wideband 180° hybrid. Attenuators AT1 and AT2 were used to equalize the individual noise spectra observed on the spectrum analyzer. At the output labeled DC, the detector current generated by either the LED or the laser was obtained.

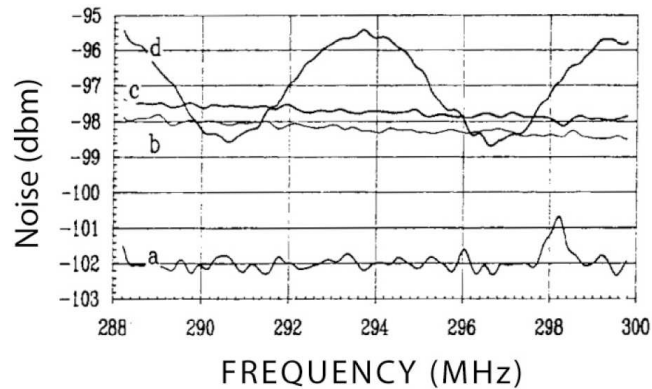


Figure 7.16: Curve *c*, the SQL produced by the LED; curve *b*, laser photon-number noise; curve *a*, junction-voltage fluctuation; and curve *d*, combined signal. In all the traces the respective dark noise levels were subtracted and the spectrum repeatedly filtered with a Gaussian of full width 81 kHz. Resolution bandwidth of the spectrum analyzer was 100 kHz and the video bandwidth was 30 Hz. The pump level was $r=9.6$.

7.4 Single Photon Turnstile Device

The previous sections concentrated on the intensity noise squeezing and quantum correlation in a pn junction light emitter in the macroscopic limit, where the charging energy due to a single carrier is negligible compared to the characteristic thermal energy. This section will describe pn junctions operating in the mesoscopic limit, where a single-carrier injection event completely suppresses the rate for a subsequent carrier-injection event.

Figure 7.17(a) shows the schematic band diagram of the mesoscopic double barrier p-i-n junction under consideration. The active region is an intrinsic GaAs QW (central QW) in the middle of a pn junction. Electrons and holes are supplied to the central QW from side QWs on the n-side and p-side, respectively, via resonant tunneling across a tunnel barrier. The n-side and p-side QWs are not deliberately doped, but carriers are supplied from nearby n-type and p-type layers by modulation doping. The lateral size of the device is assumed to be made small, in order to increase the single charging energy $q^2/2C_i$, where C_i ($i = n$ or p) is the tunnel barrier capacitance between the central QW and the i -side QW. The most important difference of the mesoscopic p-i-n junction shown in Fig. 7.17 from the macroscopic pn junction discussed in the previous sections is that it is biased by a low-impedance constant voltage source instead of a high-impedance constant current source.

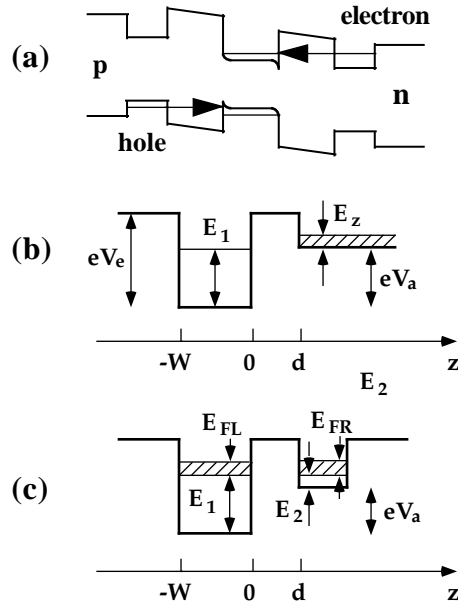


Figure 7.17: (a) Schematic energy-band diagram of the p-i-n junction structure under consideration. (b) Parameters for the tunneling matrix element calculation. (c) In the real device, the n-type lead is replaced with a second quantum well (QW)

7.4.1 Coulomb Blockade Effect on Resonant Tunneling

The electron and hole resonant tunneling rates can be uniquely determined if the quasi-Fermi level of the central QW, as well as those for the n- and p-side QWs, are given. The quasi-Fermi levels for the n- and p-side QWs can be assumed to have fixed values even immediately after electron/hole tunneling events, since the carriers are constantly supplied from highly doped layers nearby which are connected to the low-impedance constant voltage source. The quasi-Fermi level for the central QW depends on the number of carriers in the QW.

For a pn junction with such a small junction area the capacitance between the central QW and the side QWs is very small, and the charging energy associated with such a small capacitance can be significant. As an extra electron tunnels into the central QW, the capacitor between the central QW and the n-side QW becomes discharged by q . Since the total bias voltage across the pn junction is fixed by the external constant voltage source, such change in the charge configuration results in the rearrangement of the voltage drop across the tunnel barriers. Simple analysis shows that when an extra electron tunnels into the central QW, the voltage drop across the n-side barrier decreases by $q/(C_n + C_p)$, while that across the p-side barrier increases by the same amount.

This voltage rearrangement can simply be viewed as all of the energy levels of the central QW shifting upwards by $q^2/(C_n + C_p)$. In terms of the resonant tunneling rates, this means that the electron resonant tunneling rate curve is shifted upwards by $q/(C_n + C_p)$ in applied bias voltage, while the hole resonant tunneling rate curve is shifted downwards by the same amount when an extra electron tunnels. Such a shift can be understood easily by the Coulomb interaction: since the central QW now carries more negative charge, the Coulomb repulsive interaction makes it more difficult for electrons to tunnel, while the Coulomb attractive interaction makes it easier for the holes to tunnel. This shift is only sensitive to the total charge in the central QW. When a hole tunnels, it neutralizes one electron and the curves shift in the opposite directions.

- Electron and hole resonant tunneling rate curves as a function of bias voltage have the shape shown in Fig. 7.18.
- As the bias voltage is increased, the electron resonant tunneling condition is satisfied first.
- When an electron tunnels, the electron resonant tunneling rate curve shifts upwards in applied bias voltage by $q/(C_n + C_p)$, while the hole resonant tunneling rate curve shifts downwards by the same amount.
- When a hole tunnels, the resonant tunneling rate curves shift in the opposite direction.
- The shift of the resonant tunneling rate curves are sensitive only to the total charge in the central QW. Photon emission does not change the charge state, so there is no shift in the resonant tunneling rate curves associated with photon emission.

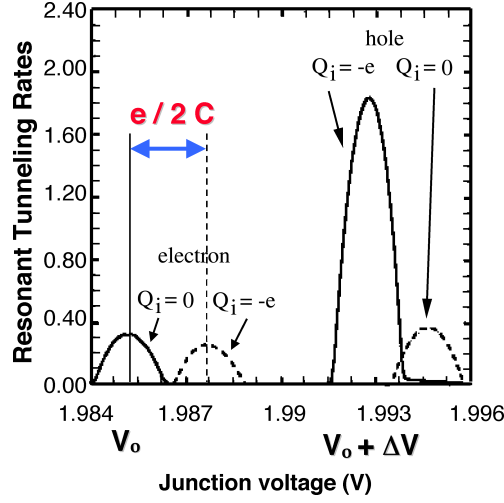


Figure 7.18: Resonant tunnel rates for electrons and holes vs. junction voltage in a mesoscopic pn junction.

7.4.2 Coulomb Staircase

Let us consider the DC operation of a double-barrier $p-i-n$ junction under constant voltage bias condition. In the ideal case where nonradiative recombination is absent, current flows through the device only by radiative recombination of electron-hole pairs in the central QW. This is possible only if both carrier (electrons and holes) tunneling events are present. At a given DC bias voltage, the electrons charge up the central QW (and move the electron tunneling rate curves up and hole tunneling rate curves down) until no more electron tunneling is allowed due to Coulomb blockade effect. If, at this voltage, the hole tunneling rate is zero, current does not flow. One needs to increase the DC voltage further to approach the hole tunneling rate curve until the electron and hole tunneling rate curves meet at the DC bias voltage, as shown in Fig. 7.19. In this figure, it is assumed that both electron and hole resonant tunnel curves are considerably broad and overlap with each other. The rising edges of the electron and hole resonant tunneling rate curves are exaggerated, and the hole resonant tunneling rate curve has a larger slope.

When the DC bias voltage is lower than point A, the hole tunneling is not allowed with $m - 1$ electrons in the central QW (where the electron and hole tunneling rates are given by the solid lines in Fig. 7.19). Once the DC bias voltage exceeds point A (with $m - 1$ electrons in the central QW), the m th electron tunneling is allowed with a finite probability and the tunneling rate curves shift to the broken lines (m electrons in the central QW). As soon as this electron tunnels, further electron tunneling is completely suppressed, while the hole tunneling rate becomes very high. A hole tunnels immediately, and the resonant tunneling rate curves return to the solid lines. In this case, electron tunneling is the slowest process that initiates the current flow, and hole tunneling follows immediately. In the limit that the hole tunneling rate is very large, so that the average waiting time for hole tunneling is completely negligible, electron injection becomes a random Poisson

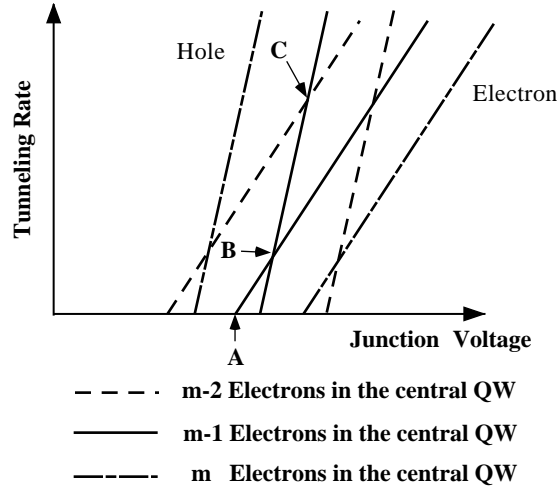


Figure 7.19: Schematic carrier dynamics for observation of the Coulomb staircase in DC I - V characteristics. The *broken lines*, *solid lines* and *dashed lines* are electron and hole resonant tunneling rates when m , $m - 1$ and $m - 2$ electrons are present in the central quantum well (QW), respectively

point process and photon emission becomes completely random. The average DC current is proportional to the electron tunneling rate, given by

$$I(V) = e R_e(V, m - 1) \quad , \quad (7.69)$$

where $R_e(V, m - 1)$ denotes the electron tunneling rate at voltage V when the central QW is populated with $m - 1$ electrons.

As the bias voltage is increased above point B, both electron and hole can tunnel, but the hole tunneling rate is now larger than the electron tunneling rate. Occasionally an (the m th) electron tunneling occurs first, in which case the current flows by the same mechanism as between points A and B discussed above. Most of the time a hole tunnels first, and the electron and hole resonant tunneling rate curves shift to the dashed lines (with $m - 2$ electrons in the central QW). Further hole tunneling is completely suppressed, and the electron tunneling rate becomes higher. An electron tunneling will follow, and the tunneling rate curves are shifted back to the solid lines. Since the hole tunneling rate (given by the solid line) is smaller than the electron tunneling rate (given by the dashed line) between points B and C, the hole tunneling triggers the current flow in this case, and electron tunneling follows immediately. The average DC current in this section is proportional to the hole tunneling rate, and is given by

$$I(V) = e R_h(V, m - 2) \quad , \quad (7.70)$$

where $R_h(V, m - 2)$ denotes the hole tunneling rate at voltage V when there are $m - 2$ electrons in the central QW. Since this curve has a larger slope compared to the hole

resonant tunneling rate curve, the I - V curve features a steep linear increase. Since hole tunneling is a Poisson point process, photon emission is not regulated.

When the bias voltage is increased above point C, a hole tunneling event (rate given by the solid line) occurs much faster than electron can tunnel (rate given by the dashed line), and the device is mostly waiting for an electron to tunnel and shift the resonant tunneling curves back to the solid lines. Once the electron tunnels, a hole tunnels immediately afterwards. The current is triggered by an electron again and features a slow linear increase following the dashed electron tunneling rate curve.

Therefore, the I - V characteristics of such a device under DC bias voltage condition feature staircase-like behavior, alternating between a slow slope for the electron tunneling rate curve and a steep slope for the hole tunneling rate curve. The steps reflect the fact that the number of electrons in the central QW decreases by 1 and appear every time the bias voltage is increased by e/C_p . The height of the steps (in current) is determined by the slope of the resonant tunneling rate curve. This is very similar to the situation in an asymmetric M-I-M-I-M double tunnel junction, where the Coulomb staircase was first observed[15],[16]. The requirement is that slopes on the rising edges of the resonant tunneling rate curves are different. Although the example presented in this section treats the case where the hole resonant tunneling rate curves have a steeper slope, a similar argument applies to the case where the electron tunneling rate has a steeper slope.

Next let us consider the case where an AC square-wave voltage signal with amplitude ΔV and frequency $f = 1/T$ (T is the period) is added on top of the DC bias voltage. Unlike the DC voltage bias case, since the junction voltage is modulated between V and $V + \Delta V$, the current starts to flow at a voltage before the electron and hole tunneling rate curves start to overlap. The situation is shown schematically in Fig. 7.20, where electron tunneling occurs at the voltage V and hole tunneling occurs at voltage $V + \Delta V$. We further assume that the hole resonant tunneling rate curve has a sharp rising edge, so that the hole tunneling rate multiplied by the half period is always much larger than one ($R_h(V, k)T/2 \gg 1$, where k is the number of electrons in the central QW). This guarantees that the net electron number in the central QW is reset to the initial value during the on-pulse voltage, $V + \Delta V$, every modulation cycle, and the junction operation is purely determined by the electron tunneling conditions. Under such assumption, there are two regimes of operation, depending on the frequency of the AC modulation voltage signal. In this section, the high-frequency limit is considered, where frequency is high (the period is short) so that the tunneling probability of an electron during the off-pulse duration is much smaller than unity ($R_e(V, k)T/2 \ll 1$).

Figure 7.20(a) shows the situation where the junction voltage is modulated between V_0 and $V_0 + \Delta V$. When the voltage is at V_0 , the central QW is filled with $k - 1$ electrons, and further electron tunneling is suppressed. At $V_0 + \Delta V$ the hole tunneling rate curve is not reached and no holes are allowed to tunnel; thus, one sees no current flowing through the device.

When the DC bias voltage is slightly increased to V_1 , an (the k th) electron is now allowed to tunnel at V_1 (Fig. 7.20(b)). However, the operation frequency is high, and the electron tunneling probability during the off-pulse duration satisfies $R_e(V_1, k-1)T/2 \ll 1$. Whether the electron tunnels or not, the tunneling rate curves are set to an identical condition (solid lines) each time the junction voltage is switched to $V_1 + \Delta V$ since the (first) hole tunneling probability at the on-pulse is close to unity when the electron tunnels

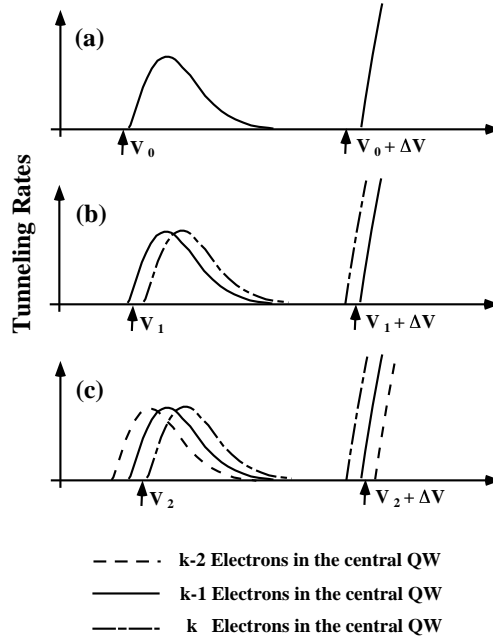


Figure 7.20: Schematic carrier dynamics for observation of the Coulomb staircase in DC + AC I - V characteristics. The *broken lines*, *solid lines* and *dashed lines* are electron and hole resonant tunneling rates when k , $k - 1$ and $k - 2$ electrons are present in the central quantum well (QW), respectively

(broken lines for k electrons in the central QW) and is zero when the electron does not tunnel (solid lines with $k - 1$ electrons). Therefore, the current is determined by the fraction of periods where an electron tunnels multiplied by the frequency of the modulation input, given by

$$I = eR_e(V_1, k - 1)/2 \quad . \quad (7.71)$$

The factor $1/2$ simply reflects the fact that electron tunneling is allowed for only half of the modulation period. In this case, the current increases linearly with increasing DC bias voltage and is independent of the AC frequency.

When the DC bias voltage is further increased to V_2 and exceeds the rising edge of the hole tunneling rate curve with $k - 1$ electrons in the central QW, the first hole is allowed to tunnel during the on-pulse (at $V = V_2 + \Delta V$) with close to unity probability (Fig. 7.20(c)). Then, the resonant tunneling rate curves for both electrons and holes shift to the dashed lines (with $k - 2$ electrons in the central QW), and when the junction voltage is decreased to V_2 , the electron tunneling rate is now given by the dashed line, which is higher than the solid line. Since the operation frequency is high, the $(k - 1)$ th and $(k - 2)$ th electron tunneling probabilities satisfy $R_e(V_2, k - 1)T/2 \ll R_e(V_2, k - 2)T/2 \ll 1$, and most of the time only one electron tunnels. Since $R_e(V_2, k - 2) > R_h(V_2 + \Delta V, k - 1)$ the current is now given by

$$I = eR_h(V_2 + \Delta V, k - 2)/2 \quad . \quad (7.72)$$

The transition between Fig. 7.20(b) and c occurs as the voltage for the on-pulse crosses a sharp rising edge of the hole resonant tunneling rate curve and the I - V characteristics feature a step-like increase.

A similar increase in the electron tunneling rate is expected whenever another electron is compensated by the addition of a hole to the central QW, due to the shift in the tunneling rate curves. Just like in the DC voltage bias case, the steps in the I - V characteristics occur at voltage values where an additional hole is added to the central QW and the corresponding current values are determined by the change in electron tunneling rate when a hole is added to the central QW. Therefore, the value of the current step is independent of the modulation frequency.

7.4.3 Turnstile Operation

When the frequency of the AC square modulation is slow so that the electron tunneling rate integrated over the off-pulse duration is much larger than unity ($R_e(V, k)T/2 \gg 1$, where k is the number of electrons in the central QW), electrons are guaranteed to tunnel into the central QW during the off-pulse. When additional electrons are added to the central QW, the shift of the tunneling rate curve due to Coulomb blockade effect causes the tunneling rate to change dramatically, so that the tunneling probability is completely suppressed, i.e., $R_e(V, k - n)T/2 \ll 1$ where n is the number of electrons that are required to tunnel before further electron tunneling is completely suppressed. This is a regime where the number of carriers injected per modulation period is well defined due to the Coulomb blockade effect.

Figure 7.21(a) shows the case where the junction voltage is modulated between V_0 and $V_0 + \Delta V$. At V_0 , $k - 1$ electrons are present in the central QW, and the tunneling rate curves are given by the solid lines. When the junction voltage is increased to $V_0 + \Delta V$ by the AC modulation voltage, it is not high enough to hit the hole resonant tunneling rate curve for $k - 1$ electrons in the central QW, and no hole tunneling occurs. Therefore, no current flows through the device.

When the DC voltage is increased slightly, as shown in Fig. 7.21(b), the k th electron tunnels at a bias voltage of V_1 . The schematic band diagram under this bias condition is shown in Fig. 7.22(a). Since the modulation frequency is low and the electron tunneling rate integrated over the off-pulse duration is large, the k th electron tunnels into the central QW. The resonant tunneling rate curves for electrons and holes shift to the broken lines for k electrons in the central QW. Once this electron tunnels, the tunneling rate for the next electron is reduced close to zero, and further electron tunneling is suppressed. When the junction voltage is increased to $V_1 + \Delta V$, hole tunneling is allowed, as shown schematically in Fig. 7.22(b). Just like in the previous section, it is assumed that the hole tunneling rate at $V_1 + \Delta V$ is large enough so that the probability of the first hole tunneling during the on-pulse duration is close to unity. A single hole tunneling event neutralizes one electron in the central QW and shifts the tunneling rate curves back to the solid lines ($k - 1$ electrons in the central QW). Further hole tunneling is suppressed during the on-pulse duration. This first hole recombines with an electron in the central QW and emits a single photon.

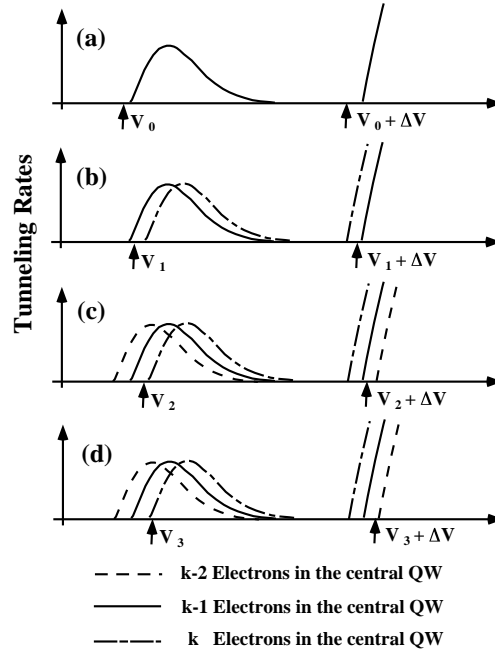


Figure 7.21: Schematic carrier dynamics in the turnstile operation regime when the junction is biased with a DC + AC voltage source in the low-frequency limit. The *broken lines*, *solid lines* and *dashed lines* are electron and hole resonant tunneling rates when k , $k - 1$ and $k - 2$ electrons are present in the central quantum well (QW), respectively

When the DC junction voltage is further increased (so that $V_2 + \Delta V$ allows a hole to tunnel with $k - 1$ electrons in the central QW) as in Fig. 7.21(c), two holes are allowed to tunnel during the duration of the on-pulse ($V = V_2 + \Delta V$) with close to unity probability. After the two holes tunnel, the tunneling rate curves move to the dashed lines ($k - 2$ electrons in the central QW), and further hole tunneling is suppressed. When the junction voltage is decreased to V_2 , two electrons are allowed to tunnel (with probability close to unity, since the second electron tunneling rate is also large) before further electron tunneling is suppressed. After two electrons tunnel, the charge state of central QW is returned to the initial condition. This will result in the emission of two photons per modulation cycle.

A similar argument can be applied to the three-hole tunneling case. A schematic of this operation is given in Fig. 7.21(d). We note that when the frequency of the AC modulation signal is low the number of electrons and holes injected per modulation period is very well defined, since the electron and hole tunneling probabilities are either close to unity or completely suppressed. This gives rise to well-defined plateaus in the I - V curve, with each plateau corresponding to $I = nef$. The transition between two adjacent plateaus is rather sharp, since it is determined by the slope of the rising edge in the electron and hole tunneling rate curves. Since the number of electrons and holes injected per modulation

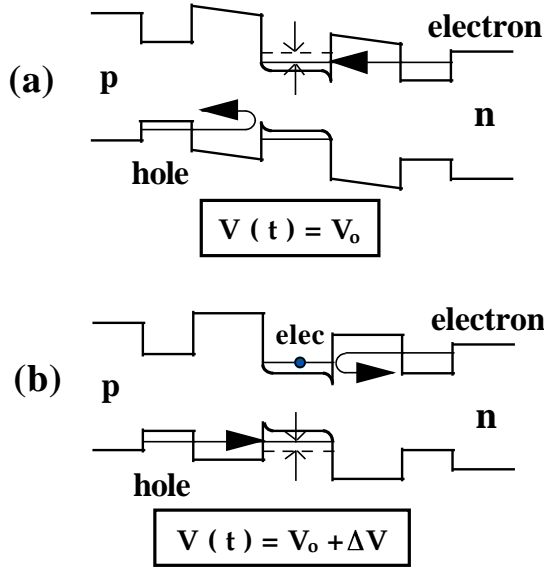


Figure 7.22: Schematic operation of a single-photon turnstile device, with one electron and one hole injected per modulation period

period, the number of photons emitted per modulation period, is a well-defined number.

A mesoscopic pn junction that operates in this regime with $n = 1$ is called a single-photon turnstile device[4]. It is worth noting that a broad resonant tunneling linewidth opens up the possibility for multiple-photon generation per modulation period[5].

Figure 7.23 shows the measured dc current as a function of AC modulation frequency for a mesoscopic $p-i-n$ junction device with a diameter of 600 nm. A fixed AC amplitude of 72 mV is superposed on the three different DC voltages, $V = 1.545, 1.547$ and 1.550 V. As the modulation frequency was increased, the DC current increased linearly as a function of the modulation frequency. The measured current was in close agreement with the relation $I = ef$, $I = 2ef$, and $I = 3ef$ (solid lines). In Fig. 7.24, the slopes I/f from the current versus frequency curves were evaluated and plotted as a function of the DC bias voltage. It is seen that the slope increases discretely, creating plateaus at $I/f = ne$, where $e = 1.6 \times 10^{-19}$ C is the charge of an electron and $n = 1, 2$ and 3 .

The locking of the current at multiples of the modulation frequency ($I = nef$) suggests that the charge transfer through the device is strongly correlated with the external modulation signal. At the first current plateau, $I = ef$, a single (the m th) electron and a single (the first) hole are injected into the central QW per modulation period, resulting in single-photon emission. At the second current plateau, $I = 2ef$, two [the m th and $(m + 1)$ th] electrons and two (the first and second) holes are injected into the central QW per modulation period, resulting in two-photon emission. Similarly at the third current plateau, $I = 3ef$, three electrons and three holes are injected per modulation period, resulting in three-photon emission. This multiple charge operation becomes possible because of relatively broad inhomogeneous linewidths of the n -side and p -side QWs.

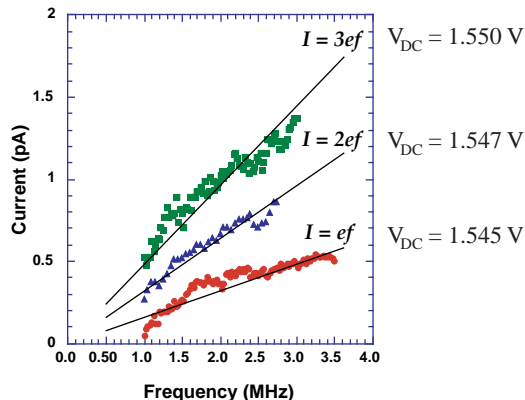


Figure 7.23: The modulation frequency dependence of the DC current in the 600 nm turnstile device. The background DC (leakage) current, which is independent of the modulation frequency, has been subtracted. The measured current agrees with the relation $I = nef$ (*solid lines*), where e is the electron charge and $n = 1, 2$ and 3

The histograms of the measured time delay between photon detection and on-pulse rising edge, with 10 MHz modulation frequency, is shown in Fig. 7.25(a) (for $I = ef$) and Fig. 7.25(c) (for $I = 2ef$). The solid line on top indicates the external AC modulation voltage, and the finite photon counts during the off-pulse period are due to the dark counts of the detector. For the $I = ef$ plateau, a photon is emitted after the rising edge of the pulse since a single electron is injected at V_0 and a single hole is injected at $V_0 + \Delta V$. The photon-emission probability has a peak near the rising edge of the modulation input. The rapid increase of the photon-emission probability is associated with the hole tunneling time ($\tau_h \simeq 4$ ns), and the slow decay of the photon-emission probability corresponds to the radiative recombination lifetime ($\tau_{ph} \simeq 25$ ns). When only one electron and one hole are allowed to be injected and only one photon is emitted per modulation cycle, the photon-emission probability $P(t)$ for the time t after the turn-on of a higher voltage pulse is given by

$$P_1(t) = \frac{\exp(-t/\tau_{ph}) - \exp(-t/\tau_h)}{\tau_{ph} - \tau_h} \quad , \quad (7.73)$$

where τ_{ph} is the radiative recombination lifetime and τ_h is the tunneling time of the hole. The dashed line is generated by this analytical formula using the parameters τ_h and τ_{ph} found from the experiment. Photon-emission probability in Fig. 7.25(a) decays to a non-zero value during the on-pulse due to photons generated by background current. The ratio of the counts contained in the peak to those contained in the non-zero background is $\sim 3:1$, consistent with the ratio of the turnstile current to the background current in this device. Figure 7.25(b) shows the Monte-Carlo numerical simulation performed for this situation; it reproduces the experimental result well.

For the $I = 2ef$ plateau shown in Fig. 7.25(c), the photon-emission probability dis-

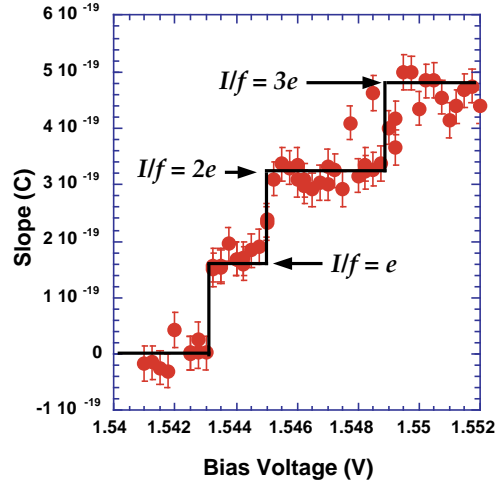


Figure 7.24: The slopes I/f in the current–frequency curve versus DC bias voltage. The slopes I/f are quantized and forms plateaus at multiples of e , indicating operation at $I = ef$, $2ef$ and $3ef$

tribution is broader, since two electrons and two holes are injected, and two photons are generated per modulation period. The photon-emission probability for the case where two electrons and two holes are allowed to tunnel can also be calculated analytically, as

$$\begin{aligned}
 P_2(t) &= \frac{2\tau_{ph} - \tau_{h2}}{2(\tau_{ph} - \tau_{h1})(\tau_{ph} - \tau_{h2})} \exp(-t/\tau_{ph}) \\
 &+ \frac{2\tau_{h1} - \tau_{h2}}{2(\tau_{h1} - \tau_{h2})(\tau_{h1} - \tau_{ph})} \exp(-t/\tau_{h1}) \\
 &+ \frac{\tau_{h2}}{2(\tau_{h2} - \tau_{h1})(\tau_{h2} - \tau_{ph})} \exp(-t/\tau_{h2}) \quad . \quad (7.74)
 \end{aligned}$$

Here, τ_{h1} is the tunneling time for the first hole and τ_{h2} is the (longer) tunneling time for the second hole. This theoretical curve is shown as a dashed line in Fig. 7.25(c). The sharp cutoff of photon emission after the falling edge of the modulation input is caused by the decay of the hole population due to simultaneous radiative recombination and reverse hole tunneling. The associated lifetime for this decay is $(\tau_h^{-1} + \tau_{ph}^{-1})^{-1}$. The experimental results as well as the analytical traces are well reproduced by the Monte-Carlo numerical simulation, as shown in Fig. 7.25(d).

In order to compare this with photons from a classically modulated macroscopic light-emitting diode, a control experiment is necessary where the Coulomb blockade effect is absent. Figure 7.25(e) shows the measured histogram of a time delay for a larger-area device (diameter of $1.4 \mu m$) at higher temperature (4 K). In this case, an arbitrary number of holes are allowed to tunnel into the central QW during an on-pulse, and so the resulting photon-emission probability should increase monotonically to a steady-state value. This

result is well-reproduced by the simulation, as shown in Fig. 7.25(f). An analytical solution for the photon- emission probability can be found, and is given by

$$P_3(t) = \frac{C}{\tau_h} [1 - \exp(-t/\tau_{ph})] \quad , \quad (7.75)$$

where C is a normalization constant. This analytical solution was used to generate the dashed lines in Fig. 7.25(e) and f. The photon-emission probability increases monotonically through the duration of the on-pulse with the time constant τ_{ph} , as one would expect from a turn-on of a classical photon source. The radiative recombination time is shorter in this case ($\simeq 5$ ns) due to a higher carrier density under the operating conditions.

7.5 Quantum Dot Single Photon Source

A single photon turnstile device requires a cryogenic operational temperature of ~ 50 mK to satisfy the condition $q^2/2C_{dep} \gg k_B\theta$. If an electron-hole pair is trapped in a quantum dot with a lateral size of $\lesssim 50$ nm, the strong Coulomb interaction between charged particles in a quantum dot differentiates the emission wavelengths for the last photon, second last photon and so on. By post-filtering the 1st photon with an appropriate wavelength filter, a single photon is extracted for every pump pulse. This was demonstrated first by optical pumping [17, 18] and later by electrical pumping [19]. It was also confirmed that those single photons are quantum mechanically indistinguishable particles so that they feature a bosonic quantum interference effect [20]. The details of those subjects are described by the following publications.

7.5.1 Triggered Single Photons from a Quantum Dot

See the attached publication; "Triggered Single Photons from a Quantum Dot", C. Santori et al., PRL 86, 1502 (2001).

7.5.2 Indistinguishable Photons from a Single-Photon Device

See the attached publication; "Indistinguishable photons from a single-photon device", C. Santori et al., Nature 419, 594 (2002).

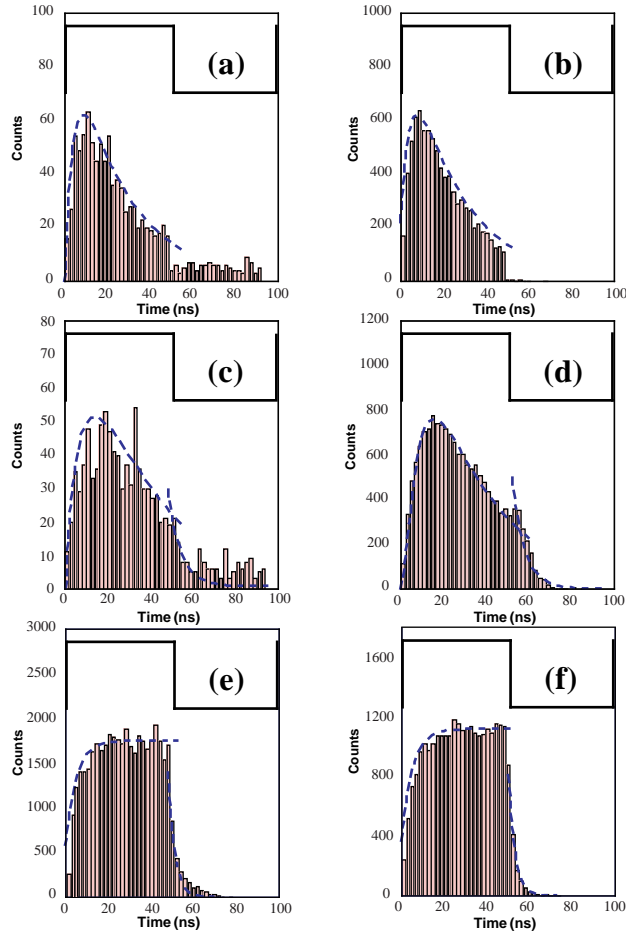


Figure 7.25: Photon-emission characteristics of the turnstile device. (a) Measured histogram of the time delay between the rising edge of the modulation input and the photon-detection event at the first plateau ($I = ef$). (b) Monte-Carlo numerical simulation result for the first plateau. (c) Measured histogram of a time delay at the second plateau ($I = 2ef$). (d) Monte-Carlo numerical simulation result for the second plateau. (e) Measured histogram of a time delay for a larger-area device (diameter of $1.4 \mu\text{m}$) at higher temperature (4 K), where the Coulomb blockade effect is absent. (f) Monte-Carlo numerical simulation result for this modulated classical light-emitting diode case

Bibliography

- [1] A. Imamoglu and Y. Yamamoto, *Phys. Rev. Lett.* **70**, 3327 (1993).
- [2] J. Kim, H. Kan, and Y. Yamamoto, *Phys. Rev. B* **52**, 2008 (1995).
- [3] A. Imamoglu, Y. Yamamoto, and P. Solomon, *Phys. Rev. B* **46**, 9555 (1992).
- [4] A. Imamoglu and Y. Yamamoto, *Phys. Rev. Lett.* **72**, 210 (1994).
- [5] J. Kim, O. Benson, H. Kan, and Y. Yamamoto, *Nature* **397**, 500 (1999).
- [6] S. M. Sze, *Physics of Semiconductor Devices*, (Wiley, New York, 1981).
- [7] A. W. Hull and N. H. Williams, *Phys. Rev.* **25**, 147 (1925); B. J. Thomson, D. O. North, and W. A. Harris, *RCA Rev.* **4**, 269 (1939).
- [8] W. H. Richardson and Y. Yamamoto, *Phys. Rev. Lett.* **66**, 1963 (1991).
- [9] S. Machida, Y. Yamamoto, and Y. Itaya, *Phys. Rev. Lett.* **58**, 1000 (1987).
- [10] P. R. Tapster, J. G. Rarity, and J. S. Satchell, *Europhysics Letters* **4**, (1987).
- [11] R. S. Muller and T. I. Kamins, *Device Electronics for Integrated Circuits, 2nd edn.* (Wiley, New York, 1986).
- [12] J. Kim, H. Kan, and Y. Yamamoto, *Phys. Rev. B* **52**, 2008 (1995).
- [13] Y. Yamamoto and S. Machida, *Phys. Rev. A* **35**, 5114 (1987).
- [14] S. Machida, Y. Yamamoto, and Y. Itaya, *Phys. Rev. Lett.* **58**, 1000 (1987); S. Machida and Y. Yamamoto, *Phys. Rev. Lett.* **60**, 792 (1988).
- [15] J. B. Barner and S. T. Ruggiero, *Phys. Rev. Lett.* **59**, 807 (1987).
- [16] T. A. Fulton and G. J. Dolan, *Phys. Rev. Lett.* **59**, 109 (1987).
- [17] O. Michler et al., *Science* **290**, 2282 (2000).
- [18] C. Santori et al., *Phys. Rev. Lett.* **86**, 1502 (2001).
- [19] Z. Yuan et al., *Science* **295**, 102 (2002).
- [20] C. Santori et al., *Nature* **419**, 594 (2002).

Triggered Single Photons from a Quantum Dot

Charles Santori, Matthew Pelton, Glenn Solomon,* Ysulte Dale, and Yoshihisa Yamamoto[†]

Quantum Entanglement Project, ICORP, JST, E. L. Ginzton Laboratory, Stanford University, Stanford, California 94305
(Received 9 October 2000)

We demonstrate a new method for generating triggered single photons. After a laser pulse generates excitons inside a single quantum dot, electrostatic interactions between them and the resulting spectral shifts allow a single emitted photon to be isolated. Correlation measurements show a reduction of the two-photon probability to 0.12 times the value for Poisson light. Strong antibunching persists when the emission is saturated. The emitted photons are also polarized.

DOI: 10.1103/PhysRevLett.86.1502

PACS numbers: 42.50.Dv, 73.21.La, 78.67.Hc

Photons from classical light sources, which usually consist of a macroscopic number of emitters, follow Poisson statistics or super-Poisson statistics [1]. With a single quantum emitter, however, one can hope to generate a regulated photon stream, containing one and only one photon in a given time interval. Such an “antibunched” source would be useful in the new field of quantum cryptography, where security from eavesdropping depends on the ability to produce no more than one photon at a time [2,3].

Continuous streams of antibunched photons were first observed from single atoms and ions in traps [4,5]. More recently, experiments demonstrating triggered single photons have used single molecules as the emitters, excited optically either by laser pulses [6,7] or through adiabatic following [8].

Solid-state sources have potential advantages. Most importantly, they may be conveniently integrated into larger structures, such as distributed-Bragg-reflector microcavities [9,10] to make monolithic devices. In addition, most do not suffer from the photo-bleaching effect that severely limits the lifespan of many molecules. The first experimental effort towards a solid-state single-photon source was based on electrostatic repulsion of single carriers in a semiconductor micropost *p-i-n* structure [11]. Milli-Kelvin temperatures were required, however, and sufficient collection efficiency to measure the photon correlation function was not obtained. More recently, continuous antibunched fluorescence has been seen from color centers in a diamond crystal [12,13] and from CdSe quantum dots [14].

Our method to generate triggered single photons involves pulsed optical excitation of a single quantum dot and spectral filtering to remove all but the last emitted photon. Optically active quantum dots confine electrons and holes to small regions so that their energy levels are quantized [15]. If several electrons or holes are placed in the dot at the same time, they will, to a first approximation, occupy single-particle states as allowed by the Pauli exclusion principle. However, electrostatic interactions between the particles cause perturbations in the eigenstates and energies. For example, if two electron-hole pairs (excitons) are created (a “biexcitonic” state), the first pair to recombine emits at a slightly lower energy than the second pair,

due to a net attractive interaction [16,17]. We exploit this effect to generate single photons not only through regulated absorption, as in the single-molecule experiments, but also through this emission property, that the last photon to be emitted after an excitation pulse has a unique wavelength, and therefore can be spectrally separated from the others.

A sample was fabricated containing self-assembled InAs quantum dots surrounded by a GaAs matrix [15]. The dots were grown by molecular beam epitaxy (Fig. 1a) at a high temperature to allow alloying with the surrounding GaAs, thereby shortening the emission wavelength. They were then capped by 75 nm of GaAs. Mesas about 120 nm tall, 200 nm wide, and spaced 50 μm apart were fabricated by electron-beam lithography and dry etching. The dots are sparse enough ($11 \mu\text{m}^{-2}$) that the smallest mesas contain, on average, fewer than one dot.

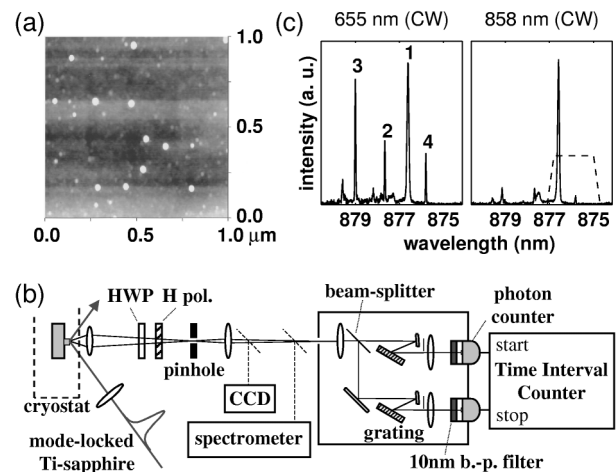


FIG. 1. (a) Atomic force microscope image of uncovered InGaAs self-assembled quantum dots, grown under identical conditions to those used in this experiment. (b) The experimental setup, showing the laser-excited sample (left), collection optics (middle left), and Hanbury Brown and Twiss-type configuration (right). (c) Emission spectra from a quantum dot under above-band excitation (left) and resonant excitation (right). The dotted line indicates approximately the portion of the spectrum that reaches the photon counters after filtering.

The experimental setup is shown in Fig. 1b. The sample was cooled to 5 K in a cryostat and placed close to the window. A mode-locked Ti-sapphire laser with 2.9 ps pulses and a 76 MHz repetition rate was focused onto a mesa from a steep (53.5° from normal) angle, down to an $18 \mu\text{m}$ effective spot diameter. Emission from the dot inside the mesa was collected with an $\text{NA} = 0.5$ aspheric lens and focused onto a pinhole that effectively selected a $5 \mu\text{m}$ region of the sample for collection. A rotatable half-wave plate followed by a horizontal polarizer selected a particular linear polarization. The light was then sent to a charge-coupled device camera, a spectrometer, or a Hanbury Brown and Twiss-type configuration for measuring the photon correlation function. Two EG&G “SPCM” photon counters were used for detection, with efficiencies of 40% at 877 nm, and 0.2-mm-wide active areas. A monochromator-type configuration defined a 2-nm-wide measurement bandwidth, with the center wavelength determined by the detector position. Additional rejection of unwanted light (scattered pump light and stray room light) was obtained with a 10 nm bandpass filter attached to each detector. The electronic pulses from the photon counters were used as start (t_1) and stop (t_2) signals for a time interval counter, which recorded these intervals $\tau = t_2 - t_1$ as a histogram.

Mesas containing single dots were identified by their optical emission spectra. The mesa chosen for this experiment contains a dot whose main ground-state emission wavelength is 876.4 nm. With continuous-wave (cw) excitation above the GaAs band gap, the emission spectrum (Fig. 1c, left) displays several lines, as has been reported elsewhere [18]. We believe that these lines all come from a single dot because another mesa shows a nearly identical emission pattern (peak heights, spacings, and widths), except for an overall wavelength shift, suggesting that this pattern is not random. To avoid ionization of the dot or delayed capture of electrons and holes, we tuned the laser wavelength to an absorption resonance at 857.5 nm, thus creating excitons directly inside the dot. With resonant excitation, emission peaks 3 and 4 almost disappear (Fig. 1c, right), and therefore we believe that they represent emission from other charge states of the dot [19]. We identify peak 1 as ground-state emission after the capture of a single exciton, and peak 2 as biexcitonic emission after the capture of two excitons. This assignment is supported by the dependence of the emission line intensities on pump power (Fig. 2a), showing linear growth of peak 1 and quadratic growth of peak 2 in the weak pump limit. A biexcitonic energy shift of 1.7 meV is seen.

Under pulsed, resonant excitation, a clear saturation behavior is seen for peak 1 (Fig. 2b). Although peak 2 and its surrounding peaks (presumably multiple-excitonic emission) continue to grow as the pump power is increased, peak 1 reaches a maximum value, since only the last exciton to recombine emits at this particular wavelength. This is shown quantitatively in Fig. 2c. Here, a photon counter

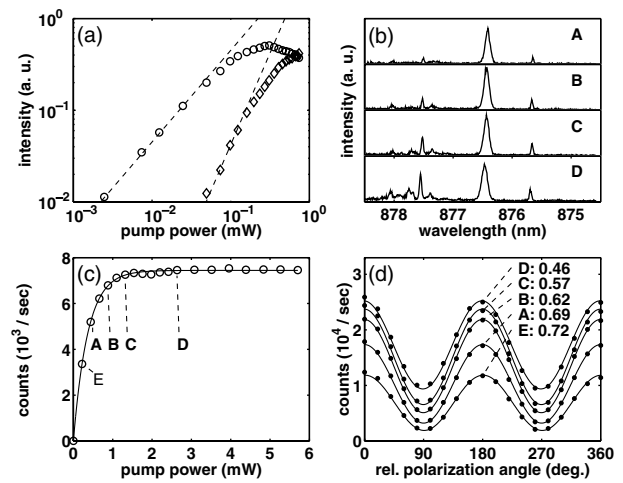


FIG. 2. (a) A log-log plot of emission line intensity versus above-band (cw) pump power, showing linear growth of peak 1 (circles) and quadratic growth of peak 2 (diamonds). (b) Emission spectra, (c) emission intensity (measured under the filtering condition depicted in Fig. 1b), and (d) emission polarization dependence of the dot under pulsed, resonant excitation with powers $E, A-D$: 0.22, 0.44, 0.88, 1.32, and 2.63 mW, respectively. The count rates in (c) are further reduced by an additional bandpass filter. The solid line in (c) is a least-squares fit of Eq. (1), while the solid lines in (d) fit a sinusoid plus an offset, resulting in the shown visibilities $(\max - \min)/(\max + \min)$.

was used to measure the emission rate versus pump power, with the detection band tuned to accept peak 1 but reject peak 2 (see dashed line, Fig. 1c). A simple saturation function for unregulated absorption that fits the data well is

$$I = I_0(1 - e^{-P/P_{\text{sat}}}), \quad (1)$$

where I is the measured intensity for single-exciton emission, P is the pump power, and I_0 and P_{sat} are fitting parameters that characterize the total collection efficiency and the absorption rate, respectively.

The emission from peak 1 was also linearly polarized. Since the degree of polarization of the emission depended strongly on the pump polarization angle, we believe that the effect is largely due to the selection rules for photon absorption and emission [20,21]. The polarization of a pump photon is transferred into the spin of an exciton, and if no spin relaxation occurs, the spin is transferred back to the emitted photon polarization. The polarization is linear, as would be expected for asymmetric dots under no magnetic field [22,23]. At the optimal pump polarization used in this experiment, emission polarization with up to 72% visibility was observed at weak pump (Fig. 2d). The lack of perfect visibility was perhaps due to spin relaxation, imperfect selection rules, or effects of the post geometry. The visibility was partially degraded when the pump power was increased into the saturation regime.

We next examine the photon correlation function, $g^{(2)}(\tau)$, which contains information on photon emission statistics [1]. For a pulsed source, $g^{(2)}(\tau)$ becomes a

series of peaks separated by the laser repetition period, and the areas of these peaks give information on photon number correlations between pulses separated by time τ . Of special interest is the central peak at $\tau = 0$, which gives an upper bound on the probability that two or more photons are emitted from the same pulse:

$$2P(n_j \geq 2)/\langle n \rangle^2 \leq \frac{1}{T} \int_{-\epsilon}^{\epsilon} g^{(2)}(\tau) d\tau, \quad (2)$$

where n_j is the number of photons in pulse j , ϵ is chosen to include the entire central peak in the integration region, and T is the pulse repetition period. This result, along with $g^{(2)}(\tau)$, is independent of the collection and detection efficiencies. For a “classical” (Poisson) source, the normalized central peak area [right-hand side of Eq. (2)] is one.

Histograms of the time interval $\tau = t_2 - t_1$ taken at four different pump powers are shown in Fig. 3. In the limit of low collection and detection efficiency (≈ 0.0003 combined in our case), these histograms, after correct normalization, approximate the photon correlation function. The peaks are broader than the limit imposed by the photon counter timing resolution (0.3 ns) and indicate a lifetime for the single-exciton state of about 0.7 ns. The $\tau = 0$ peak shows a large reduction in area, indicating strong antibunching. The numbers printed above the peaks indicate the peak areas, properly normalized by dividing the histogram areas by both singles rates, the laser repetition period, and the measurement time. For the numbers shown, the only background counts subtracted were those due to the known dark count rates of the photon counters (130 and

180 s^{-1}), almost negligible compared to the singles rates, 19 800 and 14 000 s^{-1} for the two counters at 0.88 mW pump power. When only counts within 2.8 ns of $\tau = 0$ were included, a normalized $g^{(2)}(\tau = 0)$ peak area of 0.12 was obtained at 0.88 mW. Subtracting the constant background floor seen in the data gave an even lower value of 0.095.

The observed antibunching has two causes. The first cause is a suppression of the probability for the dot to absorb a second photon after the first photon has been absorbed. If one collects emission from both the single-exciton and multiexciton lines, the $g^{(2)}(\tau = 0)$ peak area is still reduced to about 0.32 due to limited absorption. A possible explanation for reduced absorption of the second photon is that electrostatic interactions, similar to those responsible for the 1.7 meV biexcitonic energy shift, move the absorption resonance to a lower energy for the second photon [24]. The second cause for the observed antibunching is that, even if more than one exciton is created, only the last exciton to recombine emits at our collection wavelength. Under these collection conditions, we see a fair degree of antibunching at all pump wavelengths, even above band, if the pump power is not too high. The remaining counts seen at $\tau = 0$ under optimal pump and collection conditions are most likely due to imperfect filtering to reject multiexcitonic emission.

While the central correlation peak area is reduced, the adjacent peaks have normalized areas larger than one. This indicates positive correlations between the detected photon numbers from adjacent pulses. This longer-term bunching behavior is better seen in Fig. 4, which plots normalized correlation peak areas versus peak number over a longer time span. The extra peak area above one is seen to decay exponentially away from $\tau = 0$. For larger pump powers,

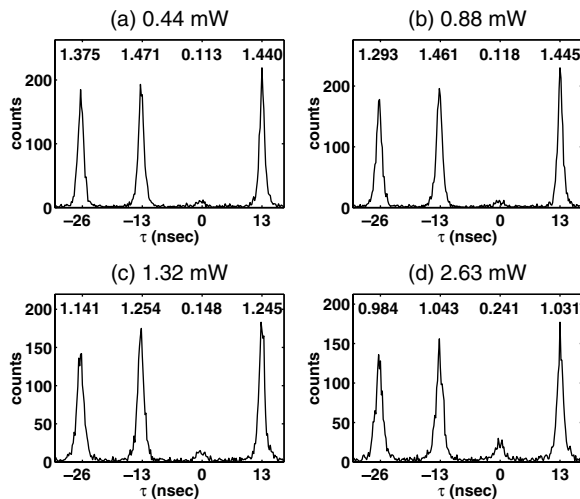


FIG. 3. Histograms of the time intervals $\tau = t_2 - t_1$ between photons detected by the “start” and “stop” counters, for four different excitation powers: (a) 0.44 mW, (b) 0.88 mW, (c) 1.32 mW, and (d) 2.63 mW. The numbers printed above the peaks give the normalized correlation peak areas, calculated using a 5.6-ns-wide integration window. The reduction of the $\tau = 0$ peak demonstrates antibunching.

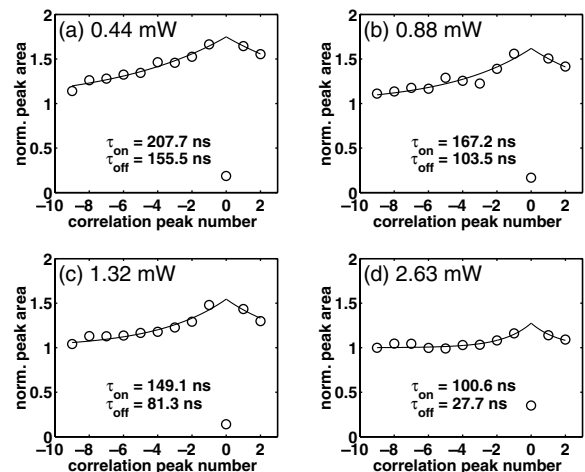


FIG. 4. Normalized correlation peak areas (13-ns-wide integration window) obtained from longer time-scale histograms, plotted against peak number, counted from $\tau = 0$, for four different excitation powers: (a) 0.44 mW, (b) 0.88 mW, (c) 1.32 mW, and (d) 2.63 mW. The lines are least-squares fits using Eq. (3), and the fitting parameters obtained are shown.

the time scale and the magnitude of the effect decrease. A simple model to describe this behavior assumes that the dot randomly “blinks” between two conditions, a fully functioning condition and a “dark” (or wavelength-shifted) condition in which photons are not observed, with time constants τ_{on} and τ_{off} . This model results in

$$h_{m \neq 0} = 1 + \frac{\tau_{\text{off}}}{\tau_{\text{on}}} e^{-(1/\tau_{\text{off}} + 1/\tau_{\text{on}})|mT|}, \quad (3)$$

where h_m is the m th normalized correlation peak area, and T is the laser repetition period. Fitting this model to the data gives the values for τ_{on} and τ_{off} shown on the plots, which are on the order of 100 ns. Long-term (>1 s) blinking behavior has already been reported in strain-induced GaAs dots [25] and InP dots [26], and emission wavelength fluctuations have been reported for InGaAs dots [27]. These effects have been attributed to nearby defects [26] and trapped charges [27]. The more rapid blinking behavior seen here is unwanted and necessarily decreases the efficiency of the device, but it should be contrasted with the bleaching behavior of single molecules. The quantum dot described here has been studied for months and cooled down to 5 K about 30 times without ceasing to function or changing significantly.

In summary, we have demonstrated a new method for generating triggered single photons, using a single quantum dot excited on resonance by laser pulses. The method takes advantage of Coulomb interactions between excitons and the resulting spectral shifts to isolate single emitted photons. We observed a tenfold two-photon probability suppression and strongly polarized emission, suggesting that a single quantum dot is a promising candidate for a practical single-photon source, although some unwanted blinking was also observed. The main remaining challenge is to improve the collection efficiency, which we expect can be accomplished by growing a microcavity around the dot.

We thank S. Somani for loaning critical equipment. Financial assistance for C. S. was provided by the National Science Foundation. Financial assistance for C. S. and M. P. was provided by Stanford University.

Note added.—After submission of this work, another demonstration of a single-photon source based on pulsed optical excitation of a quantum dot was reported [28]. Our work and this work were performed independently.

*Also at Solid-State Photonics Laboratory, Stanford University, Stanford, CA.

[†]Also at NTT Basic Research Laboratories, Atsugishi, Kanagawa, Japan.

- [1] D. F. Walls and G. J. Milburn, *Quantum Optics* (Springer-Verlag, Berlin, 1994).
- [2] G. Brassard, N. Lütkenhaus, T. Mor, and B. Sanders, *Phys. Rev. Lett.* **85**, 1330 (2000).
- [3] G. Brassard and C. Crépeau, *SIGACT News* **27**, 13 (1996).
- [4] H. J. Kimble, M. Dagenais, and L. Mandel, *Phys. Rev. Lett.* **39**, 691 (1977).
- [5] F. Diedrich and H. Walther, *Phys. Rev. Lett.* **58**, 203 (1987).
- [6] F. De Martini, G. Di Giuseppe, and M. Marrocco, *Phys. Rev. Lett.* **76**, 900 (1996).
- [7] B. Lounis and W. E. Moerner, *Nature (London)* **407**, 491 (2000).
- [8] C. Brunel, B. Lounis, P. Tamarat, and M. Orrit, *Phys. Rev. Lett.* **83**, 2722 (1999).
- [9] B. Ohnesorge *et al.*, *Phys. Rev. B* **56**, R4367 (1997).
- [10] J. M. Gérard *et al.*, *Phys. Rev. Lett.* **81**, 1110 (1998).
- [11] J. Kim, O. Benson, H. Kan, and Y. Yamamoto, *Nature (London)* **397**, 500 (1999).
- [12] C. Kurtsiefer, S. Mayer, P. Zarda, and H. Weinfurter, *Phys. Rev. Lett.* **85**, 290 (2000).
- [13] R. Brouri, A. Beveratos, J.-P. Poizat, and P. Grangier, *Opt. Lett.* **25**, 1294 (2000).
- [14] P. Michler *et al.*, *Nature (London)* **406**, 968 (2000).
- [15] D. Bimberg *et al.*, *Quantum Dot Heterostructures* (John Wiley & Sons, Chichester, 1999). For MBE growth of InAs self-assembled dots, see Chap. 4.2.
- [16] A. Kuther *et al.*, *Phys. Rev. B* **58**, R7508 (1998).
- [17] M. Bayer, O. Stern, P. Hawrylak, S. Fafard, and A. Forchel, *Nature (London)* **405**, 923 (2000).
- [18] L. Landin, M. S. Miller, M.-E. Pistol, C. E. Pryor, and L. Samuelson, *Science* **280**, 262 (1998).
- [19] R. J. Warburton *et al.*, *Nature (London)* **405**, 926 (2000).
- [20] Y. Toda, S. Shinomori, K. Suzuki, and Y. Arakawa, *Phys. Rev. B* **58**, R10 147 (1998).
- [21] H. Gotoh, H. Ando, H. Kamada, A. Chavez-Pirson, and J. Temmyo, *Appl. Phys. Lett.* **72**, 1341 (1998).
- [22] D. Gammon, E. S. Snow, B. V. Shanabrook, D. S. Katzer, and D. Park, *Phys. Rev. Lett.* **76**, 3005 (1996).
- [23] M. Sugisaki *et al.*, *Phys. Rev. B* **59**, R5300 (1999).
- [24] This is consistent with our observation that, if the pump wavelength is tuned 1.7 meV below the first-photon resonance, strong photon bunching [$g^2(0)$ enhancement factor of about 3.5] occurs. In this case, the energy shift brings the second-photon absorption closer to resonance.
- [25] D. Bertram, M. C. Hanna, and A. J. Nozik, *Appl. Phys. Lett.* **74**, 2666 (1999).
- [26] M.-E. Pistol, P. Castrillo, D. Hessman, J. A. Prieto, and L. Samuelson, *Phys. Rev. B* **59**, 10725 (1999).
- [27] H. D. Robinson and B. B. Goldberg, *Phys. Rev. B* **61**, R5086 (2000).
- [28] P. Michler *et al.*, *Science* **290**, 2282 (2000).

Indistinguishable photons from a single-photon device

Charles Santori^{*}, David Fattal^{*}, Jelena Vučković^{*}, Glenn S. Solomon^{*†} & Yoshihisa Yamamoto^{*‡}

^{*} Quantum Entanglement Project, ICORP, JST, E. L. Ginzton Laboratory, Stanford University, Stanford, California 94305-4088, USA

[†] Solid-State Photonics Laboratory, Stanford University, Stanford, California 94305-4085, USA

[‡] NTT Basic Research Laboratories, Atsugi, Kanagawa, 243-0198, Japan

Single-photon sources have recently been demonstrated using a variety of devices, including molecules^{1–3}, mesoscopic quantum wells⁴, colour centres⁵, trapped ions⁶ and semiconductor quantum dots^{7–11}. Compared with a Poisson-distributed source of the same intensity, these sources rarely emit two or more photons in the same pulse. Numerous applications for single-photon sources have been proposed in the field of quantum information, but most—including linear-optical quantum computation¹²—also require consecutive photons to have identical wave packets. For a source based on a single quantum emitter, the emitter must therefore be excited in a rapid or deterministic way, and interact little with its surrounding environment. Here we test the indistinguishability of photons emitted by a semiconductor quantum dot in a microcavity through a Hong–Ou–Mandel-type two-photon interference experiment^{13,14}. We find that consecutive photons are largely indistinguishable, with a mean wave-packet overlap as large as 0.81, making this source useful in a variety of experiments in quantum optics and quantum information.

When identical single photons enter a 50–50 beam splitter from opposite sides, quantum mechanics predicts that both photons must leave in the same direction, if their wave packets overlap perfectly. This two-photon interference effect originates from the Bose–Einstein statistics of photons. This bunching effect was first observed using pairs of highly correlated photons produced by parametric downconversion¹⁴, but it should also occur with single, independently generated photons. Most proposed applications for single-photon sources in the field of quantum information (with the notable exception of quantum cryptography¹⁵) involve two-photon interference. Such applications include quantum teleportation¹⁶, post-selective production of polarization-entangled photons¹⁷, and linear-optics quantum computation¹². It is therefore important to demonstrate that consecutive photons emitted by a single-photon source are identical and exhibit mutual two-photon interference effects.

The experiment described here used a semiconductor quantum dot as the photon source. Quantum dots are attractive as single-photon sources because they are relatively stable, have narrow spectral linewidths and rapid radiative decay rates, and can be integrated into larger fabricated structures—such as microcavities—to improve the collection efficiency^{18,19}. A quantum dot excited on resonance by a pulsed source can have an extremely small probability of generating two photons in the same pulse—as required for this experiment. Furthermore, recent reports have indicated coherence times²⁰, and even time-averaged linewidths^{21,22}, fairly close to the radiative limit in some cases, suggesting that dephasing is slow, and thus indistinguishable photons may be achievable.

Our sample contains self-assembled InAs quantum dots (about 25 μm^{-2}) embedded in GaAs and sandwiched between distributed-Bragg-reflector (DBR) mirrors, grown by molecular-beam epitaxy¹⁹. Pillars (Fig. 1a) with diameters ranging from 0.3 to 5 μm and heights of 5 μm were fabricated in a random distribution by chemically assisted ion beam etching (CAIBE), using sapphire dust particles as etch masks. The resulting microcavities, exhibiting

three-dimensional photon confinement, have quality factors of approximately 1,000 and measured spontaneous-emission rate enhancement (Purcell) factors as high as 5. Many pillars with only one or two quantum dots on resonance with a fundamental cavity mode were found. The sample was cooled to 3–7 K in a cryostat. To generate single photons, we focused 3-ps pulses from a Ti-sapphire laser every 13 ns onto these pillars from a steep angle. The laser was tuned to an excited-state absorption resonance of the quantum dot, typically 20–30 nm shorter in wavelength than the first-level emission wavelength. The quantum-dot emission was collected, and a single polarization was selected. The emission was then spectrally filtered with a resolution of about 0.1 nm using a diffraction grating, and coupled into a single-mode fibre.

By this method, we obtained bright, single-photon sources with excellent two-photon suppression and negligible background emission. We have chosen three quantum dots for this study, denoted as dots 1, 2 and 3, with emission wavelengths (in nm) of 931, 932 and 937, respectively. A photon-correlation measurement for dot 2 is shown in Fig. 1b. A parameter often used to quantify two-photon suppression is $g^{(2)}$, the probability of generating two photons in the same pulse, normalized by an equally bright Poisson-distributed source. We estimate $g^{(2)} = 0.053, 0.067$ and 0.071 for dots 1, 2 and 3, respectively. But for the experiment described below, the important parameter is the probability of generating two photons in the same pulse, for either of two consecutive pulses, divided by the

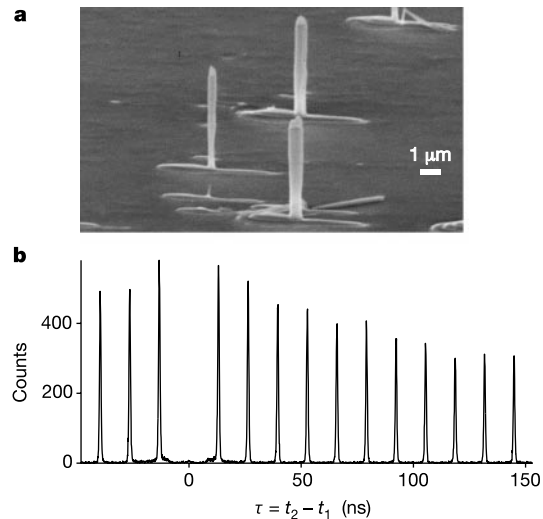


Figure 1 The single-photon source. **a**, Pillar microcavity structures containing InAs quantum dots in a one-wavelength-thick GaAs spacer, sandwiched between distributed-Bragg-reflector (DBR) mirrors, grown by molecular-beam epitaxy. The DBR mirrors were constructed by stacking quarter-wavelength-thick GaAs and AlAs layers on top of each other. There are 12 DBR pairs above, and 30 DBR pairs below, the spacer. Pillars with diameters ranging from 0.3 to 5 μm and heights of 5 μm were fabricated in a random distribution by chemically assisted ion beam etching (CAIBE) with Ar^+ ions and Cl_2 gas, using sapphire dust particles as etch masks. Owing to the irregular shapes of the pillars, the fundamental mode is typically polarization-nondegenerate. **b**, Photon correlation histogram of emission from quantum dot 2 under pulsed, resonant excitation, obtained using a Hanbury Brown and Twiss-type set-up. The emission was split into two paths by a beam splitter, each path leading to a photon counter. A histogram was generated of the relative delay $\tau = t_2 - t_1$ between a photon detection at one counter (t_1) and the other (t_2). The vanishing central peak is the signature of suppressed two-photon emission. The parameter g described in the text was obtained by dividing the area of the central peak at $\tau = 0$ by that of the nearest side peaks. The decrease of the side peaks away from $\tau = 0$ indicates blinking with a timescale of 85 ns, an effect that we usually see with resonant excitation⁹. For this measurement, the set-up shown in Fig. 3a was used, with one arm blocked.

probability of generating one photon in each pulse. We estimate this quantity to be $g = 0.039, 0.027$ and 0.025 for quantum dots 1, 2 and 3, respectively. The difference between $g^{(2)}$ and g is due to blinking in our source.

Two other properties of the quantum-dot emission are also important for the two-photon interference experiment described below: the spontaneous emission lifetime and the coherence length. The average emission intensity of quantum dots 1, 2 and 3 is plotted versus time after an excitation pulse, measured under resonant excitation by a streak camera (Fig. 2a). By fitting decaying exponential functions, we estimate the spontaneous emission lifetimes τ_s of dots 1, 2 and 3 to be (in ps) 89, 166 and 351, respectively. This variation is due largely to differences in how well each quantum dot couples to its microcavity. A Michelson interferometer is used to measure the coherence length of the time-averaged emission (Fig. 2b). The curves show how the interference fringe contrast varies with path-length difference, and give the magnitude of the Fourier transform of the intensity spectra. When we did not select a single polarization, we sometimes observed oscillatory behaviour due to polarization splitting of the emission lines²³. For dots 2 and 3 (with splittings of 13 and 17 μeV), we were able to eliminate this effect by selecting a particular linear polarization. For dot 1, the 45- μeV splitting could not easily be eliminated, probably because the quantum-dot emission couples to just one cavity mode having a polarization rotated $\sim 45^\circ$ relative to the splitting axis of the quantum dot. We estimate the $1/e$ coherence lengths τ_c (divided by c) for quantum dots 1, 2 and 3 to be (in ps) 48, 223 and 105, respectively. Quantum dot 2 is closest to being Fourier-transform-

limited, with $2\tau_s/\tau_c = 1.5$. When this ratio is equal to 1, no dephasing can be present, and perfect two-photon interference is expected.

The main elements of the two-photon interference experiment are shown in Fig. 3a. The single-photon source is as described above, except that the quantum dot is excited twice every 13 ns by a pair of equally intense pulses with 2 ns separation. Two pulses, each containing zero or one photons, emerge from the single-mode fibre. They are split into two arms by a beam splitter, with one arm ($2 \text{ ns} + \Delta t$) longer than the other. The beams then recombine at a different place on the same beam splitter. The two outputs of this interferometer are collected by photon counters, and a photon correlation histogram is generated of the relative delay time $\tau = t_2 - t_1$ for two-photon coincidence events, where t_1 and t_2 are the times at which photons are detected at detectors 1 and 2, respectively. A histogram obtained in this way for dot 2 with $\Delta t = 0$ is shown in Fig. 3b.

Five peaks appear within the central cluster, corresponding to three types of coincidence events. For peaks 1 and 5 at $\tau = \mp 4 \text{ ns}$, the first photon follows the short arm of the interferometer, the second photon follows the long arm, and one photon goes to each counter. For peaks 2 and 4 at $\tau = \mp 2 \text{ ns}$, both photons follow the same arm. For peak 3 at $\tau = 0$, the first photon follows the long arm, and the second photon follows the short arm, so that the two photons collide upon their second pass through the beam splitter. Only in this case can two-photon interference occur, and for perfect two-photon interference, peak 3 vanishes.

When the source successfully delivers a pair of photons, the two-

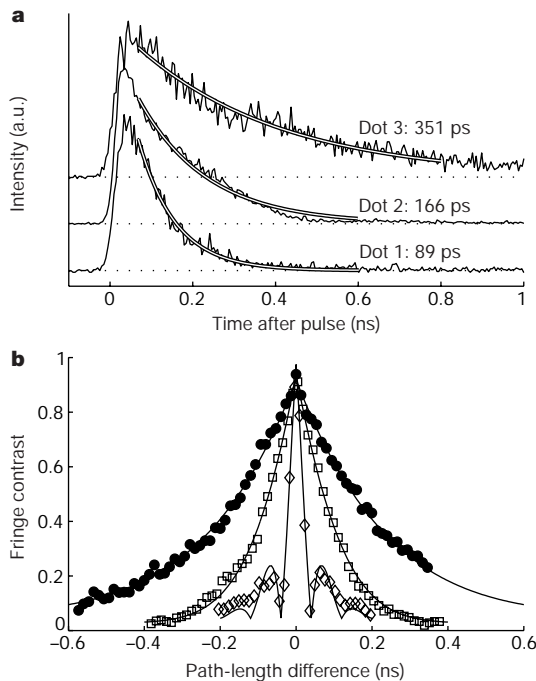


Figure 2 Time-averaged emission properties of quantum dots 1, 2 and 3. **a**, Spontaneous emission decay under resonant excitation, measured by a streak camera. By fitting exponentials, lifetimes τ_s of 89, 166 and 351 ps for dots 1, 2 and 3, respectively, are obtained. **b**, Coherence length, measured using a Michelson interferometer, showing fringe contrast versus path-length difference. The set-up was similar to the one shown in Fig. 3a, but with the 2-ns delay removed. The fringe contrast was measured by monitoring the intensity of one of the interferometer outputs while varying one of the arm lengths over several wavelengths using a piezoelectric transducer. The arm length was then moved over long distances by a motor stage. The $1/e$ coherence lengths τ_c are 48, 223 and 105 ps for dots 1 (diamonds), 2 (filled circles) and 3 (squares), respectively.

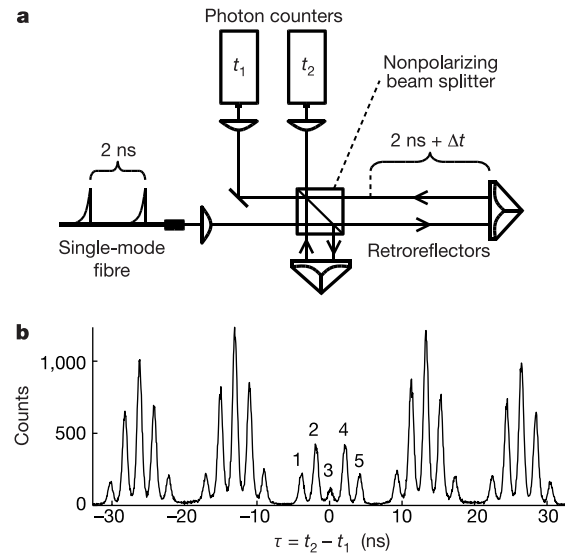


Figure 3 Two-photon interference experiment. **a**, Every 13 ns, two pulses, separated by 2 ns and containing 0 or 1 photons, arrive through a single-mode fibre. The pulses are interfered with each other using a Michelson-type interferometer with a ($2 \text{ ns} + \Delta t$) path-length difference. Corner-cube retroreflectors are used at the ends of the arms, so that the mode overlap is insensitive to slight angular misalignment of the optical elements. The length of the short arm can be adjusted over long distances by a 15-cm motor stage. The fringe contrast measured using a laser with a long coherence length was 0.92, limited by optical surface imperfections. The interferometer outputs are collected by photon counters, and the resulting electronic signals are correlated using a time-to-amplitude converter followed by a multi-channel analyser card, which generates a histogram of the relative delay time $\tau = t_2 - t_1$ between a photon detection at one counter (t_1) and the other (t_2). **b**, Such a histogram (53-ps bin size) obtained for quantum dot 2, with $\Delta t = 0$. The number of repetitions was $N = 2.3 \times 10^{10}$ (5 min), and the combined two-photon generation and detection efficiency was $\eta^{(2)} = 2.5 \times 10^{-6}$, which includes all losses in the experimental set-up. The small area of peak 3 demonstrates two-photon interference.

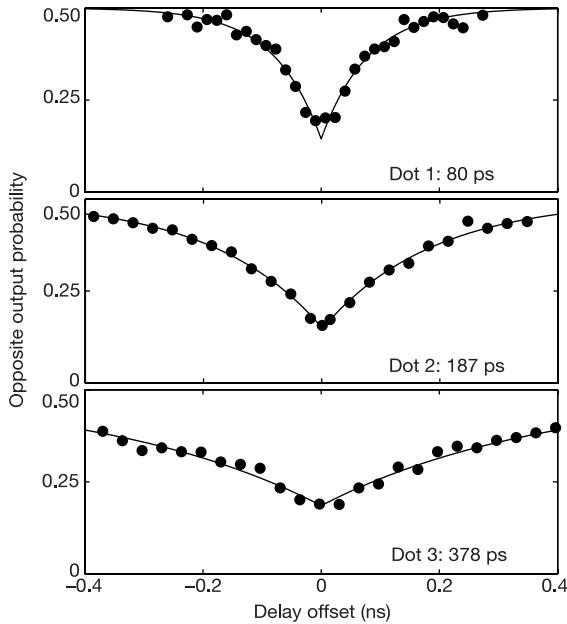


Figure 4 The probability that two photons that collide at the beam splitter leave in opposite directions, plotted as a function of interferometer delay offset, Δt . Data are shown for quantum dots 1, 2 and 3. The drops in the coincidence rate near zero offset demonstrate two-photon interference. From model fits (solid lines), the $1/e$ widths of the dips are estimated as 80, 187 and 378 ps for dots 1, 2 and 3, respectively, in close agreement with the measured spontaneous emission lifetimes.

photon state can be written as

$$|\psi\rangle = \int ds x(s) \int dt y(t) a^\dagger(s) a^\dagger(t + 2 \text{ ns}) |0\rangle \quad (1)$$

where $a^\dagger(t)$ is the photon creation operator at time t , $x(s)$ and $y(t)$ define the photon wave packets, and $|0\rangle$ is the vacuum state. We assume that the photon wave packets are much shorter than 2 ns. In the limit of low collection efficiency, the mean areas of peaks 1–5 are

$$\begin{aligned} A_1 &= N\eta^{(2)}R^3T, \quad A_2 = N\eta^{(2)}[R^3T(1 + 2g) + RT^3] \\ A_3 &= N\eta^{(2)}[(R^3T + RT^3)(1 + 2g) - 2(1 - \varepsilon)^2R^2T^2V(\Delta t)] \quad (2) \\ A_4 &= N\eta^{(2)}[R^3T + RT^3(1 + 2g)], \quad A_5 = N\eta^{(2)}RT^3 \end{aligned}$$

where N is the number of repetitions, $\eta^{(2)}$ is the combined two-photon generation and detection efficiency, and R and T are the beam-splitter intensity coefficients of reflection and transmission, respectively. As defined above, the parameter g characterizes the two-photon emission probability, with $g = 0$ for an ideal single-photon source, and $g = 1$ for a Poisson-distributed source (without blinking). The parameter $1 - \varepsilon$ is the interference fringe contrast measured when an ideal monochromatic calibration source is sent into the interferometer, and accounts for optical surface imperfections. The parameter $V(\Delta t) = \langle |\int dt x(t)y^*(t + \Delta t)|^2 \rangle$ in the expression for peak 3 is the mean overlap between the wave packets of the two photons for interferometer path-length difference ($2 \text{ ns} + \Delta t$). An ensemble average is performed over all possible two-photon states generated by the source.

The signature of two-photon interference that we observe is the small size of peak 3 in Fig. 3b, compared with peaks 2 and 4. We define the quantity $M(\Delta t) = A_3/(A_2 + A_4)$ in terms of the peak areas in equation (2). This quantity is equal to the conditional probability, given that two photons collide at the beam splitter, that the photons leave in opposite directions, in the limit $g \approx 0$. We measured $M(\Delta t)$ while varying the interferometer path length offset

Table 1 Summary of quantum-dot parameters

	$g^{(2)}$	g	τ_s (ps)	τ_c (ps)	τ_m (ps)	$V(0)$
Dot 1	0.053	0.039	89	48	80	0.72
Dot 2	0.067	0.027	166	223	187	0.81
Dot 3	0.071	0.025	351	105	378	0.74

For the three quantum dots chosen for this study, we show the conventional two-photon suppression parameter $g^{(2)}$, the ratio g of the probability of emitting two photons in either of two consecutive pulses to the probability of emitting one photon in each pulse, the spontaneous emission lifetime τ_s , the coherence length τ_c , the $1/e$ width of the Mandel dip τ_m , and the two-photon overlap at zero path-length difference $V(0)$.

Δt (Fig. 4). For all three quantum dots, we observe reductions in the coincidence probability near $\Delta t = 0$, by factors of 0.61, 0.69 and 0.62 for dots 1, 2 and 3, respectively. The remaining coincidences we see are partly due to independently measured optical imperfections in our set-up, $R/T = 1.1$ and $(1 - \varepsilon) = 0.92$. Without these imperfections, the coincidence reduction factors would be $V(0) = 0.72$, 0.81 and 0.74 for quantum dots 1, 2 and 3, respectively.

To analyse these data, we fitted the function $M(\Delta t) = 0.5[1 - a \exp(-|\Delta t|/\tau_m)]$, where the fitting parameters a and τ_m characterize the depth and the width of the coincidence dip, respectively. The fits, shown as solid lines in Fig. 4, match the data well. For an ideal spontaneous-emission source, with instantaneous initial excitation and no decoherence, a would differ from 1 only because of imperfections in the optical set-up, and τ_m would be equal to the spontaneous emission lifetime. The fitted values of τ_m we obtain (in ps) are 80, 187 and 378 for quantum dots 1, 2 and 3, respectively. These values agree quite well with the spontaneous emission decay lifetimes τ_s obtained in Fig. 2a (see also Table 1). For quantum dots 1 and 3, this result is surprising, given the short coherence lengths τ_c listed above. We conclude that, for quantum dots 1 and 3, the primary spectral broadening mechanism occurs on a timescale much longer than 2 ns. Such a ‘spectral diffusion’ effect could occur owing to charge fluctuations in the vicinity of the quantum dot, for example²².

For quantum dot 2, we calculate a mean two-photon overlap of at least 0.81. The remaining imperfection could arise from several decoherence mechanisms. When the quantum dot is first excited by a laser pulse, the generated electron–hole pair is initially in an excited state, and must relax to its lowest state through phonon emission before a photon can be emitted at the proper wavelength. The ratio of this relaxation time, which could be as long as tens of picoseconds, to the lowest-state radiative lifetime could limit the performance of this source. Decoherence by phonons^{24,25} is another possible mechanism, though we see little temperature dependence from 3 to 7 K. Finally, the spectral diffusion mechanism noted above could also potentially contribute to decoherence on short timescales.

The two-photon interference effect that we observe indicates a large enough degree of photon indistinguishability to perform interesting quantum-optical experiments. The performance of most schemes based on two-photon interference depends on the same wave-packet overlap as measured here. For example, for a single-photon implementation of a scheme to generate single pairs of polarization-entangled photons¹⁷, the polarization correlation would ideally be unity in the horizontal/vertical basis, and 0.81 in the $+45^\circ/-45^\circ$ basis, violating Bell’s inequality. We hope that other applications, such as quantum teleportation and quantum logic gates, will become feasible as the performance of single-photon sources continues to improve. □

Received 27 June; accepted 23 August 2002; doi:10.1038/nature01086.

- De Martini, E., Di Giuseppe, G. & Marrocco, M. Single-mode generation of quantum photon states by excited single molecules in a microcavity trap. *Phys. Rev. Lett.* **76**, 900–903 (1996).
- Brunel, C., Lounis, B., Tamarat, P. & Orrit, M. Triggered source of single photons based on controlled single molecule fluorescence. *Phys. Rev. Lett.* **83**, 2722–2725 (1999).
- Lounis, B. & Moerner, W. E. Single photons on demand from a single molecule at room temperature. *Nature* **407**, 491–493 (2000).

4. Kim, J., Benson, O., Kan, H. & Yamamoto, Y. A single-photon turnstile device. *Nature* **397**, 500–503 (1999).
5. Beveratos, A. *et al.* Room temperature stable single-photon source. *Eur. Phys. J. D* **18**, 191–196 (2002).
6. Kuhn, A., Henrich, M. & Rempe, G. Deterministic single-photon source for distributed quantum networking. *Phys. Rev. Lett.* **89**, 067901 (2002).
7. Michler, P. *et al.* A quantum dot single-photon turnstile device. *Science* **290**, 2282–2285 (2000).
8. Santori, C., Pelton, M., Solomon, G., Dale, Y. & Yamamoto, Y. Triggered single photons from a quantum dot. *Phys. Rev. Lett.* **86**, 1502–1505 (2001).
9. Zwiller, V. *et al.* Single quantum dots emit single photons at a time: antibunching experiments. *Appl. Phys. Lett.* **78**, 2476–2478 (2001).
10. Yuan, Z. *et al.* Electrically driven single photon source. *Science* **295**, 102–105 (2002).
11. Gérard, J.-M. & Gayral, B. Strong Purcell effect for InAs quantum boxes in three-dimensional solid-state microcavities. *J. Lightwave Technol.* **17**, 2089–2095 (1999).
12. Knill, E., Laflamme, R. & Milburn, G. J. A scheme for efficient quantum computation with linear optics. *Nature* **409**, 46–52 (2001).
13. Fearn, H. & Loudon, R. Theory of two-photon interference. *J. Opt. Soc. Am. B* **6**, 917–927 (1989).
14. Hong, C. K., Ou, Z. Y. & Mandel, L. Measurement of subpicosecond time intervals between two photons by interference. *Phys. Rev. Lett.* **59**, 2044–2046 (1987).
15. Bennett, C. H. & Brassard, G. *Proc. IEEE Int. Conf. on Computers, Systems and Signal Processing* 175–179 (IEEE, New York, 1984).
16. Bouwmeester, D., Ekert, A. & Zeilinger, A. *The Physics of Quantum Information* 49–92 (Springer, Berlin, 2000).
17. Shih, Y. H. & Alley, C. O. New type of Einstein–Podolsky–Rosen–Bohm experiment using pairs of light quanta produced by optical parametric down conversion. *Phys. Rev. Lett.* **61**, 2921–2924 (1988).
18. Moreau, E. *et al.* Single-mode solid-state single photon sources based on isolated quantum dots in pillar microcavities. *Appl. Phys. Lett.* **79**, 2865–2867 (2001).
19. Solomon, G. S., Pelton, M. & Yamamoto, Y. Single-mode spontaneous emission from a single quantum dot in a three-dimensional microcavity. *Phys. Rev. Lett.* **86**, 3903–3906 (2001).
20. Borri, P. *et al.* Ultralong dephasing time in InGaAs quantum dots. *Phys. Rev. Lett.* **87**, 157401 (2001).
21. Gammon, D., Snow, E. S., Shanabrook, B. V., Katzer, D. S. & Park, D. Homogeneous linewidths in the optical spectrum of a single gallium arsenide quantum dot. *Science* **273**, 87–90 (1996).
22. Bayer, M. & Forchel, A. Temperature dependence of the exciton homogeneous linewidth in $\text{In}_{0.60}\text{Ga}_{0.40}\text{As}/\text{GaAs}$ self-assembled quantum dots. *Phys. Rev. B* **65**, 041308(R) (2002).
23. Kulakovskii, V. D. *et al.* Fine structure of biexciton emission in symmetric and asymmetric CdSe/ZnSe single quantum dots. *Phys. Rev. Lett.* **82**, 1780–1783 (1999).
24. Besombes, L., Kheng, K., Marsal, L. & Mariette, H. Acoustic phonon broadening mechanism in single quantum dot emission. *Phys. Rev. B* **63**, 155307 (2001).
25. Fan, X., Takagahara, T., Cunningham, J. E. & Wang, H. Pure dephasing induced by exciton–phonon interactions in narrow GaAs quantum wells. *Solid State Commun.* **108**, 857–861 (1998).

Acknowledgements We thank A. Scherer and T. Yoshie for access to the CAIBE system and for their help in fabrication of the structures; J. Plant for assistance with SEM imaging; and B. C. Sanders for discussions. This work was supported in part by MURI; G.S.S. was supported by DARPA, ARO and JST.

Competing interests statement The authors declare that they have no competing financial interests.

Correspondence and requests for materials should be addressed to C.S. (e-mail: chars@stanford.edu).

Superconductivity in compressed lithium at 20 K

Katsuya Shimizu*†, Hiroto Ishikawa*, Daigoroh Takao*, Takehiko Yagi‡ & Kiichi Amaya*†

* Department of Physical Science, Graduate School of Engineering Science; and † Research Center for Materials Science at Extreme Conditions, Osaka University, Toyonaka, Osaka 560-8531, Japan

‡ The Institute for Solid State Physics, University of Tokyo, Kashiwa-shi, Chiba 277-8581, Japan

Superconductivity at high temperatures is expected in elements with low atomic numbers, based in part on conventional BCS (Bardeen–Cooper–Schrieffer) theory¹. For example, it has been predicted that when hydrogen is compressed to its dense metallic phase (at pressures exceeding 400 GPa), it will become superconducting with a transition temperature above room tempera-

ture². Such pressures are difficult to produce in a laboratory setting, so the predictions are not easily confirmed. Under normal conditions lithium is the lightest metal of all the elements, and may become superconducting at lower pressures^{3,4}; a tentative observation of a superconducting transition in Li has been previously reported⁵. Here we show that Li becomes superconducting at pressures greater than 30 GPa, with a pressure-dependent transition temperature (T_c) of 20 K at 48 GPa. This is the highest observed T_c of any element; it confirms the expectation that elements with low atomic numbers will have high transition temperatures, and suggests that metallic hydrogen will have a very high T_c . Our results confirm that the earlier tentative claim⁵ of superconductivity in Li was correct.

Previous theory⁶ has predicted that dense Li will undergo a new structural transition towards a ‘paired-atom’ phase at pressures near

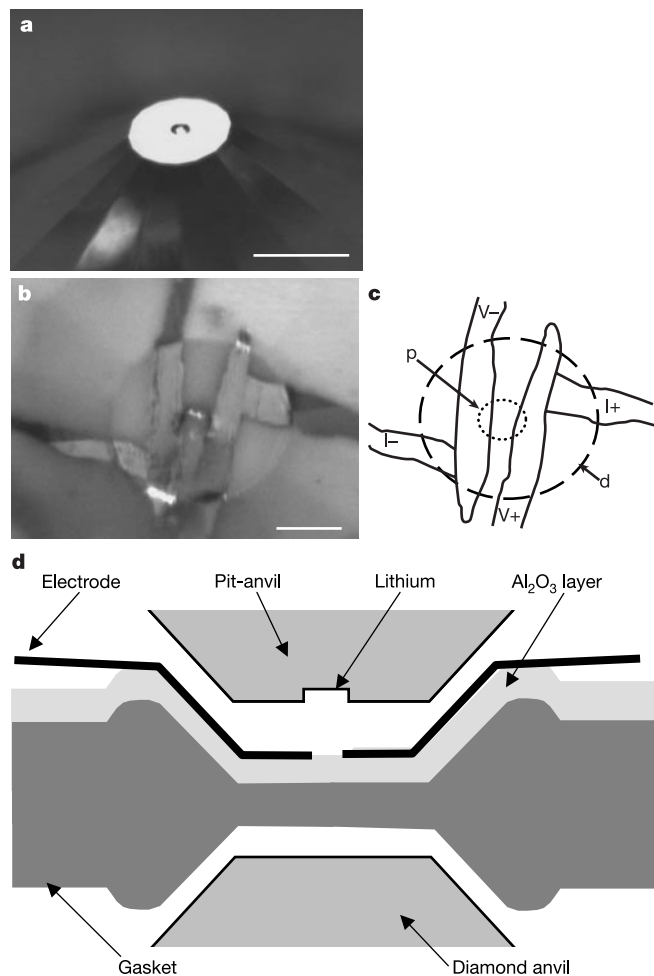


Figure 1 Arrangement of sample and electrodes on the diamond anvils. **a**, Photograph of a pit, 50 μm in diameter and 7 μm deep, on the 300- μm pressure surface of the synthetic type Ib diamond anvil. The pit was prepared by a focused ultraviolet beam from pulsed KrF-excimer laser, wavelength 248 nm. Scale bar, 0.3 mm. **b**, Electrodes on a thin aluminium oxide layer. Two platinum-film electrodes, 5- μm thick, are placed to touch the sample in the pit; scale bar, 0.1 mm. **c**, Schematic drawing of **b**. A quasi-four-wire electrical resistance measurement was performed. The measured resistivity included one of the platinum films which were placed in series connecting to the sample in the pit (p) on the diamond-anvil surface (d). A direct current of 1 mA is applied through I+ to I-, and the voltage drop between V+ and V- is recorded. **d**, Schematic drawing of the cross-section of our set-up at the top of the diamonds anvils. Ruby chips are located the bottom of the pit; the pressure was controlled by helium gas, and determined by a conventional ruby-fluorescence method through the optical windows of the cryostat.